Climatic conditions between 19 and 12 ka in the eastern Pyrenees, and wider implications for atmospheric circulation patterns in Europe

Theo Reixach, Magali Delmas, Regis Braucher, Yanni Gunnell, Cécile Mahé, Marc Calvet

Version of Record: https://www.sciencedirect.com/science/article/pii/S027737912100130X
Manuscript_e53736a94b6c251561cc00df8f723337

Climatic conditions between 19 and 12 ka in the eastern Pyrenees, and wider implications for atmospheric circulation patterns in Europe

Theo Reixach[1*], Magali Delmas[1], Régis Braucher[2], Yanni Gunnell[3], Cécile Mahé[1], Marc Calvet[1]

[1] HNHP UMR 7194, Université de Perpignan Via Domitia, Bâtiment Y 52, avenue Paul Alduy, 66860 Perpignan cedex 9, France (*theo.reixach@univ-perp.fr)
[2] CEREGE, Aix Marseille Univ., CNRS, Collège de France, IRD, INRAE, Plateau de l'Arbois 13545, Aix en Provence, France
[3] Université Lumière Lyon 2, CNRS UMR 5600, F-69676 Bron, France

Abstract. The chronology of the most extensive Late Pleistocene glaciation in the eastern Pyrenees is now well established, but climatic variations during the subsequent Last Glacial-to-Interglacial Transition (LGIT) are much less well documented. The aim of this research is to fill that gap. We present a new series of 22 ^{10}Be exposure ages from a sequence of moraines in the upper Ariège catchment, and update 64 previously published exposure ages from seven other valleys. Based on (i) geomorphological maps of successive generations of ice-marginal deposits and (ii) their age distributions, followed by (iii) glaciological modeling to infer corresponding mass-balance gradients and equilibrium line altitudes (ELAs), we reconstruct glacier behaviour in the eastern Pyrenees during the LGIT and retrieve paleoclimatic parameters for each glacial stillstand. Results document rapid deglaciation involving four relative stillstands, with an ELA rise of ~410 m and increases in temperature and precipitation of ~4 °C and ~40 %, respectively, between ~18 ka (Greenland Stadial GS-2.1b) and ~14.5 ka (Greenland Interstadial GI-1). A cold and dry environment prevailed from ~18 ka onward, and deglaciation was almost complete by GI-1. Only small glaciers persisted as late as ~12.3 ka in cirques where local conditions allowed it. These patterns are compatible with a transient Polar Front Jet Stream repositioning to latitudes of 40–42°N

between 18 and 16 ka, with Westerlies-dominated circulation not yet feeding precipitation to the mountain belt abundantly from the northwest, and outbursts of polar air meeting with cool sea waters in the western Mediterranean mostly suppressing precipitation from Mediterranean sources.

Key Words: Last Glacial-to-Interglacial Transition, deglaciation chronology, cosmogenic exposure dating, paleoclimate, modeling, Pyrenees.

1. Introduction

Fine-scale reconstructions of Holocene and Pleistocene temperature (T) and precipitation (P) conditions in terrestrial environments are best documented by biological proxies, but the mountain environments of the mid-latitudes are poorly documented by long time series. In glaciated mountains, however, glacial landforms provide a record of past glacier fluctuations from which paleoclimatic conditions can be inferred. By establishing glacial chronologies, for example based on terrestrial cosmogenic nuclide (TCN) exposure dating, and by reconstructing former mountain glaciers in three dimensions, it is possible to derive paleotemperature and paleoprecipitation conditions based on certain assumptions or analogues (e.g., Ivy-Ochs et al 2006; Biette et al., 2018; Chandler et al., 2019; Hofmann et al., 2019; Protin et al., 2019).

The circum-Mediterranean mountain ranges are particularly important testing grounds for paleoclimate studies because of their sensitivity to changes in the climatic regimes of adjacent areas, including the North Atlantic (e.g., Hughes et al., 2017). By forming a land bridge between the Atlantic Ocean in the west and the Mediterranean Sea in the east, both of which strongly influence climate along and across the mountain range, the Pyrenees offer

ideal conditions in that respect. The Late Pleistocene glaciation chronology of the Pyrenees prior to the LGM has been increasingly well documented in the last 20 years (see Delmas, 2015; Delmas et al., 2021a, b), and an emerging feature is that the time of most extensive glaciation during this last glacial cycle coincided with Marine Isotope Stage (MIS) 3 and/or MIS 4 (Jalut et al., 1992; Garcia-Ruiz et al., 2003; Lewis et al., 2009; Pallàs et al., 2010; Delmas et al., 2011; Tomkins et al., 2018). Thus, in Pyrenean valleys documented until now, the local last glacial maximum (LLGM) preceded the global last glacial maximum (LGM), which currently designates the interval from 29 ka to 19 ka (i.e., earlier part of MIS 2) and corresponds to the most recent period of maximum ice sequestration on continents worldwide (Mix et al., 2001; Thompson and Goldstein, 2006; Lambeck et al., 2014).

The inventory of Pyrenean ice-margin positions during the LGM is incomplete, but currently available data suggest a west-to-east paleoclimatic gradient along the orogen. This gradient, with maximum precipitation in the east, could be related to a southerly position of the Polar Front, which would have re-directed storm tracks and allowed Mediterranean weather systems to impinge on the eastern Pyrenees more prominently than they do now (Kuhlemann et al., 2008; Luetscher et al., 2015; Merz et al., 2015). The growing evidence in support of this scenario is based on the TCN dating record for successive generations of frontal moraines such as preserved in the Têt, Querol and Malniu valleys which, during the LGM, reached positions within a few hundred metres of their MIS 4/ MIS 3 predecessors (Pallàs et al., 2006; Delmas et al., 2008; Pallàs et al., 2010). Distances between the MIS 3/MIS 4 and LGM frontal moraines increase progressively westward, where they stand 7 km apart on the Ariège (Delmas et al., 2011) and ca. 30 km on the Gállego (Palacios et al., 2015a, 2017; Guerrero et al., 2018). A similar pattern has been reported in the European Alps, with

78 contrasts in outlet glacier lengths between the north and south foreland zones (Ivy-Ochs,
79 2015; Seguinot et al., 2018; Monegato et al., 2018; Ivy-Ochs et al., 2018), thereby suggesting
80 that southerly Mediterranean airstreams provided favorable conditions for the expansion of
81 LGM glaciers (Haeberli and Penz, 1985; Florineth and Schlüchter, 2000; Kuhlemann et al.,
82 2008; Luetscher et al., 2015; Ludwig et al., 2016; Monegato et al., 2017).
83 Testing this hypothesis more widely across western Europe calls for acquiring time
84 constraints on when circulation of the Westerlies, and thus conditions of today's prevailing
85 climates, became reestablished after the LGM. Reduced supply of moisture from the
86 Mediterranean would have sealed the fate of the Alpine glaciers, which entered a final
87 recessional phase after 22 ka and faded out after 17.5 ka (Monegato et al., 2017).
88 The chronology of glacier fluctuations in the Pyrenees since the LGM, i.e., during the Last
89 Glacial-to-Interglacial Transition (LGIT), is sparsely documented, thereby setting limits to our
90 current understanding of post-LGM paleoclimate patterns and local topoclimatic conditions.
91 Given that just a dozen sites have been radiocarbon- or TCN-dated (glaciolacustrine
92 sediments, moraines or glacially-scoured bedrock surfaces: grey and red stars in Fig. 1),
93 multiplying constraints on the chronology of the LGIT should thus be an important
94 prerequisite for deriving valid paleoclimate models for the region.
95 In this paper, we expand and refine the glacial chronology of the eastern Pyrenees (Figs. 1,
96 2), and use the record of glacier fluctuations to reconstruct climatic change during the LGIT.
97 The eastern Pyrenees host the steepest modern precipitation gradient of the entire
98 mountain belt (Fig. 2A, B). Two-thirds of the existing LGIT age determinations in the
99 Pyrenees already come from this area, with 4 in massifs on the south side of the Axial Zone
100 (Paleozoic backbone of the orogen) under Mediterranean influence (Delmas et al., 2008;

Pallàs et al., 2010; Palacios et al., 2015b; Andrés et al., 2018), and another 4 on the north side under Atlantic influence (Jalut et al., 1982; Delmas et al., 2011; Crest et al., 2017; Jomelli et al., 2020). By associating a new series of TCN ages (n = 22) for the upper Ariège catchment with recalculated TCN ages from previous work (n = 64), the aims of this paper are to (i) establish a chronology for post-LGM glacier fluctuations in the eastern Pyrenees; and (ii) derive paleoclimatic data from glaciological models of the reconstructed glaciers.

The chronological frame used in reference to cooler and warmer time intervals during the LGIT will follow the Greenland (GRIP and North GRIP) event stratigraphy (Rasmussen et al., 2014), which captures millennial-scale oscillations potentially relevant to regions bordering the North Atlantic such as the Pyrenees. The chronostratigraphic scale is based on a GS (Greenland Stadial) and GI (Greenland Interstadial) dichotomy.

2. Study area

The Pyrenees extend for ~400 km between the Atlantic Ocean and the Mediterranean Sea. The middle segment of the range hosts the highest summits, a number of them exceeding 3000 m between Mt. Balaïtous (3144 m) and Pique d'Estats (3143 m). The range at present hosts only a small number of cirque glaciers, all confined to 9 massifs where summits exceed 3000 m. Their equilibrium line altitude (ELA) is ~3200 m, thus only slightly higher than the ELA of glaciers (other than around Mont Blanc) in the Western Alps (3000–3100 m; Six and Vincent, 2014).

The eastern segment of the range (this study) displays at least three geomorphological features not encountered farther west: (i) maximum elevations do not exceed 2800–2900 m,

except for Pique d'Estats; (ii) the elevated mountain tops tend to be flat plateaus rather than serrated peaks (Calvet et al., 2015); and (iii) the mountain topography is fragmented by Neogene extensional basins (Figs. 1, 2). On the shorter and steeper north-facing side of the orogen, the Ariège catchment extends from the Axial Zone northward across belts of highly crumpled Mesozoic cover rocks containing large outposts of Paleozoic crystalline basement such as Trois-Seigneurs (summit: 2199 m), Tabe/Saint-Barthélemy (2368 m), and Arize (1716 m) massifs. The south-facing side of the Axial Zone, which also hosted Pleistocene glaciers, consists of a juxtaposition of often small watersheds, typically connecting to the Neogene intermontane half-grabens of Cerdagne, Capcir and Conflent (Figs. 1, 2). Drainage, in all cases, joins the Mediterranean either via the southern fold-and-thrust belts and Ebro Basin (Segre River); via the northern fold-and-thrust belts (Aude River); or directly eastward, mostly following the succession of Neogene tectonic breaches and basins of the Axial Zone (Têt River).

The dominant climatic characteristic of the eastern Pyrenees is the contrast between the relatively cool and humid massifs under Atlantic influence on the north side, and the much drier and somewhat warmer Mediterranean massifs in the south (Fig. 2A, B). This climatic divide occurs in the Axial Zone, near the present-day drainage divide, and is prominent in several ways. For example, south of the climatic divide the Cerdagne intermontane basin records 30 fewer rainy days and ~400 mm less mean annual precipitation than the immediately adjacent, north-facing Ariège catchment. Likewise, a steep gradient in total annual as well as daily sunshine hours distinguishes the southeastern massifs (2750 $h \cdot yr^{-1}$, with 50 % of daily sunshine in December and 70 % in July) from their northwestern counterparts (< 2000 $h \cdot yr^{-1}$, 25–30 % of daily sunshine in December and 50–55 % in July).

147 Such strong contrasts were also prevalent in the Pyrenees during the Late Pleistocene, and
148 are recorded by the north–south asymmetry in ice extent on either side of the icefield divide
149 (Fig. 2): thus, whereas on the north side quite long outlet glaciers reached the most external
150 ranges and the piedmont, on the south side glaciers never advanced beyond the Internal
151 Sierras. These differences were sharpest in the eastern Pyrenees (Delmas et al., 2011), with
152 the Ariège glacier reaching ~400 m near Foix at the time of the LLGM and collecting tributary
153 ice from the Trois-Seigneurs, Bassiès, Aston, Carlit and Tabe massifs (Figs. 1, 2). At that time,
154 the Ariège glacier was about 60 km long (ELA ca. 1800 m), whereas coeval valley glaciers in
155 the more southern massifs never exceeded 15–20 km (ELA ca. 2200 m; Fig. 2C). Post-LGM ice
156 recession was rapid on both sides of the range, occurring as early as 20 ka cal. BP in the
157 upper Têt valley (Delmas, 2005; Delmas et al., 2008) and likewise around 19–20 ka in the
158 Ariège catchment (Delmas et al., 2011). During the Glacial to Interglacial Transition, receding
159 outlet glaciers fragmented into a large number of short, disconnected cirque or valley
160 glaciers confined to the inner Axial Zone, typically 30 to 40 km from the LLGM terminal
161 moraines on the north side of the range, and 5–10 km on the south.
162
163 **3. Methods**
164 **3.1 Geomorphological mapping of glacial features**
165 Geomorphological mapping was undertaken to establish the distribution of Late
166 Pleistocene ice-marginal landforms (e.g., moraines, kame terraces) generated by stationary
167 glaciers at successive moments and locations. We used 1:25,000 scale topographic sheets
168 and high-resolution (0.2 m ground sampled distance) aerial photographs published by the
169 Institut Géographique National (IGN), and the resulting observations were completed by

ground checks and additional field surveys (see Chandler et al., 2018, for an overview of available methods). Based on the relative elevations and positions of the deposits in the catchment, the aim is to reconstruct the extent of local stadial ice margins and thus to document the relative positions of successive glacier stillstands. Benefiting from systematic field work, the geomorphological maps also report the petrographic composition of the till units in order to establish contributing areas established from 1:50,000 scale geological maps. Periglacial, paraglacial and/or postglacial landforms such as rock glaciers, talus cones and debris fans were also mapped, as well as the main ridge crests, nunataks, and Neogene 'paleic' surfaces (preglacial summit erosion surfaces, whether at any time ice-covered or not).

3.2 Surface exposure dating: sampling strategy and analytical procedure

TCN dating was used to establish the exposure age of boulder surfaces embedded in lateral or frontal moraines. We sampled large granite and gneiss boulders (long axis: 1 to 5 m), each time making sure to select at least 2 or 3 boulders on each moraine as controls on age consistency (e.g., Prud'homme et al., 2020). All samples (~2 cm thick) were taken from boulder tops that displayed features indicative of glacial abrasion (e.g., rounded, glacially-polished surfaces; Fig. 3) in order to minimise two commonly encountered risks (e.g., Heyman et al., 2011): one situation arises when the sample has retained a proportion of nuclides accumulated in the minerals prior to glaciation (so-called nuclide inheritance) because glacial denudation was overall insufficiently intense to reset the nuclide inventory to zero. This results in overestimating boulder exposure age, and thus in spuriously concluding that deglaciation occurred earlier than it actually did. The other (reverse)

193 situation arises in the case of post-glacial boulder-surface degradation (loss of rock mass,
194 and thus also of nuclides), or in the case of delayed exhumation from till matrix initially
195 shielding the boulder from direct contact with the atmosphere. This results in a relative
196 nuclide deficit in the boulder's ^{10}Be inventory, generates anomalously young exposure ages,
197 and thus spuriously underestimates the true timing of deglaciation.

198 We followed the chemical procedure of Braucher et al. (2011) for ^{10}Be extraction
199 from the quartz contained in the rock samples. The samples were crushed and sieved, the
200 250–1000 µm fraction retrieved, and magnetic minerals removed using a Frantz™
201 isodynamic magnetic separator. Chemical processing for ^{10}Be extraction consists of a
202 succession of sample dissolution steps, starting with H_2SiF_6/HCl to eliminate non-quartz
203 materials, followed by dilute HF in order to remove the atmospheric ^{10}Be. Before complete
204 dissolution in 48 % HF, samples were spiked with 0.15 g of an in-house-made ^{9}Be solution
205 (3.025±0.009 ppm; Merchel et al., 2008). After total dissolution, all sample solutions were
206 evaporated, and beryllium was extracted from the dry residues using anion and cation
207 exchange columns and precipitation of $Be(OH)_2$ in successive steps. The hydroxides were
208 dried and oxidized at 700 °C for 1 h. The BeO oxide was mixed with Nb powder and placed in
209 copper cathodes for measurement of the sample ^{10}Be/^{9}Be ratios at the French national AMS
210 facility ASTER (Arnold et al., 2010), and calibrated against in-house standard STD-11 with an
211 assigned ^{10}Be/^{9}Be ratio of (1.191±0.013) x 10^{-11} (Braucher et al., 2015) using the ^{10}Be half-life
212 of (1.387±0.0012) x 10^{6} years established by Chmeleff et al. (2010) and Korschinek et al.
213 (2010). The ^{10}Be/^{9}Be blank ratio ranged between 8.54 x 10^{-16} and 2.29 x 10^{-15}.
214 Measurement-related analytical uncertainties include ASTER counting statistics and machine
215 stability (~0.5 %; Arnold et al., 2010).

New and previously published ^{10}Be exposure ages were calculated or recalculated using the Cosmic Ray Exposure Program (CREP) (Martin et al., 2017; Suppl. Material 1). Kernel density probability age plots, which display the probability density distribution, weighted mean, and associate standard deviation of each result, were generated with the iceTEA numerical toolkit (Jones et al., 2019). All nuclide concentrations were converted to the 07KNSTD standard (Nishiizumi et al., 2007). Production rates were calibrated by applying the Lal–Stone time-corrected scaling scheme (Lal, 1991; Stone, 2000; Nishiizumi et al., 1989; Balco et al., 2008) with the muon parameters of Braucher et al. (2011), the ERA-40 atmosphere model (Uppala et al., 2005), and the ^{10}Be-based atmospheric corrections for geomagnetic field intensity (Muscheler et al., 2005), resulting in a Europe SLHL (sea-level high altitude) production rate of 4.16±0.2 at·g^{-1}·yr^{-1} (Claude et al., 2014). The SLHL was further corrected for topographic shielding (Dunne et al., 1999) and snow shielding (Gosse and Phillips, 2001) using a mean value for snow density of 0.25 g·cm^{-3}. Snow cover extrapolations are based on present-day data provided by a high-resolution model developed by Meteo-France (ANR SCAMPEI: http://www.umr-cnrm.fr/scampei/presentation_scampei/index.php). Whether newly acquired (n = 22) or recalibrated from previous publications (n = 49), the ^{10}Be results were modeled with and without snow-shielding correction in order to assess the influence of this parameter on results. Both age series were calculated under a hypothesis of no postglacial denudation given the well-rounded and glacially-polished characteristics of the sampled surfaces (Fig. 3A–D).

Recalculations of published ^{36}Cl exposure ages (n = 15) were based on the statistical tools developed by Schimmelpfennig (2009) and Schimmelpfennig et al. (2009; Suppl.

239 Material 1). Elevation–latitude scaling factors were evaluated using CosmoCalc (Vermeesch,
240 2007) and were based on the scaling models of Stone (2000) for nucleonic production, and
241 Braucher et al. (2011) for muonic contribution.
242
243 **3.3 Glaciological and paleoclimate modeling**
244 Ice-margin reconstructions and chronologies obtained from the methods described
245 above were used to characterise the paleoclimatic conditions prevalent in the glacial
246 catchment during the corresponding interval. The approach is based on the two following
247 steps, both of which interact iteratively as illustrated in Suppl. Figure 2.1.
248 The first step uses the GlaRe ArcGis™ toolbox developed by Pellitero et al. (2016) to
249 reconstruct glacier ice-thickness profiles based on a simple glaciological model, schematically
250 illustrated in Figure 4A and detailed in Suppl. Material 2. The toolbox requires as inputs (i)
251 glacier outlines, here provided by the geomorphological maps; (ii) glacier bed topography
252 (obtained in the present case from the 5 m IGN digital elevation model); and (iii) glacier
253 flowlines manually drawn based on the present-day slope system. We assumed that the
254 subglacial topography has remained roughly unchanged since the LGM.
255 The second step focuses on the reconstruction of T and P conditions that were prevalent at
256 the time of a given glacial stillstand For this, we used a Matlab script developed by Harper
257 and Humphrey (2003) and improved by Blard et al. (2007; see Suppl. Material 2). The
258 application allows a glacier mass-balance in a given climatic context to be reconstructed on
259 the basis on four parameters: (i) mean monthly temperatures (MMT) and their associated
260 standard deviation (1σ), (ii) cumulative monthly precipitation (CMP), (iii) temperature and
261 precipitation altitude gradients, and (iv) degree-day factor (*DDF*) values. The advantage of

using the two models in combination is that Harper and Humphrey (2003) impose a default shear stress of 100 Pa, whereas basal shear stress in GlaRe is a variable. Optimal fits of glacier thickness to the ice-margin deposits are thus enhanced by more realistic values of that key variable (Suppl. Table 2.1).

In this study, the climatic reference frame is elaborated from present-day CMP and MMT values recorded from the nearest 16 weather stations (see Fig. 2C and Suppl. Table 2.2). Data were normalised to a reference altitude of 1400 m based on an atmospheric annual temperature lapse rate and precipitation gradient set to 0.63 °C·100 m^{-1} and 46 mm·100 m^{-1}, respectively (López-Moreno, 2006), thus generating spatially-averaged values of CPM and MMT (see Suppl. Table 2.3). This baseline then makes it possible to investigate the magnitude of annual temperature and precipitation anomalies, ΔT and ΔP, relative to the current baseline, and thus also provides the potential for appreciating Pleistocene climatic changes through space and time.

DDF values of 3.0 mm eq. water·°C^{-1}·day^{-1} for snow, and 6.1 mm eq. water·°C^{-1}·day^{-1} for ice, were applied on the basis of the glaciological data recorded for glaciers in the western French Alps (Six and Vincent, 2014). Regional *DDF* variations are known to be a function of humidity, wind speed, and cloud cover (Hock, 2003). Uncertainty arising from these variations can be defined by a sensitivity test (Blard et al., 2007). This approach consists in estimating the uncertainty envelope around reconstructed temperatures and precipitation (ΔT, ΔP) by running the mass-balance model with extreme *DDF* input values from various temperate glaciers around the world (Braithwaite et al., 2000; Hock, 2003; see Suppl. Table 2.4). Given the ±17.8 % envelope with respect to the *DDF* value recorded for the Alpine glaciers, the sensitivity test estimates mass-balance gradient (MBG) variation

between ±0.09 and ±0.03 $m \cdot yr^{-1} \cdot 100\ m^{-1}$, resulting in uncertainties around Pyrenean paleoclimatic reconstructions of ±0.5 °C for temperatures and ±5 to ±25 % for precipitation (light blue shading in Fig. 4C).

Lastly, the mass-balance model was calibrated by modern glaciological baseline data in order to integrate orographic effects on precipitation and snow redistribution by wind and avalanches. Using 2001–2017 glaciological data from the Ossoue glacier on the north side of the central Pyrenees (source: Observatoire des Glaciers des Pyrénées françaises) and from the Maladeta glacier on the south side (source: Pedrero Muñoz, pers. comm., 2019; Fig. 1), we established that mass-balance best fits were obtained when applying an average correction factor of 2.9 to available CMP values, and that this factor was fully valid for an elevation band ranging between ~1400 m and the elevated glacier surface. The factor of 2.9 is consistent with the value of 2.8 applied by Marti (2016). Overall, the modern theoretical mass-balance gradient reconstructed for the eastern Pyrenees is thus 0.54 $m \cdot yr^{-1} \cdot 100\ m^{-1}$ with an ELA at 3163 m (red curve in Fig. 4B).

After the modern surface mass-balance curve has been established, the current MMT and CMP are changed by step-wise, user-defined perturbations aimed at making the glacier expand from present-day conditions until it reaches the desired spatial extent defined by the mapped and dated ice-margin deposits (see Section 3.1). The models combined in the Harper and Humphrey (2003) algorithm generate a large range of paleoclimatic conditions, i.e., several ΔP and ΔT pairs, each corresponding to a specific ice-thickness profile, itself related to a given mass-balance gradient and to a given altitudinal position of the ELA (smaller blue circles in Figure 4C). Ideally, output values of ΔP or ΔT should be constrained by independently obtained paleoclimate proxies. Given, however, the absence of data on past

atmospheric conditions in the study area, we used best-fitting ice thickness profiles generated by the Glare Toolbox as criteria for selecting (among the multiple solutions generated by the Harper and Humphrey model) the best-fitting values of MBG, ELA, and deviations of P and T (ΔP, ΔT) relative to present-day climatic conditions (larger blue circles in Figure 4C).

4. Results: glacier fluctuation chronology and paleoclimate reconstructions

4.1. The upper Ariège catchment

4.1.1. Sequence of ice-marginal deposits and landforms

The geomorphological maps shown in Figure 5 highlight ice-marginal deposits in two key areas: (i) along the Ariège valley, close to Petches and Mérens-les-Vals; and (ii) in the vicinity of Col de Puymorens, at the contributory outlets of the En Garcia, Orri, Baladrar and Pas-de-la-Casa subcatchments.

At the village of Petches (Fig. 5A), three lateral moraines between 900 and 960 m on the slopes of the Ariège valley mark out the successive positions of a valley glacier significantly thinner than during the LLGM, when it attained the 1650 m elevation contour in this section of the catchment (Delmas et al., 2012). The ice front is not well marked out by a frontal moraine, but the position of the lateral moraines suggests that the 25-km-long glacier reached the 800 m elevation contour at Ax-les-Thermes. At this time, the Ariège iceway was disconnected from the Najar tributary glaciers, and probably also from the Oriège (Delmas et al., 2011). Further upstream, close to Mérens, a frontal moraine at 1050 m marks out the terminal position of an even thinner and shorter glacier, 15 km long and disconnected from its Nabre and Mourguillou tributaries (Fig. 5A).

331 Although not abundant enough to qualify as moraines, conspicuous alignments of
332 glacially-polished gneiss boulders between 1950 and 1980 m striking NW–SE along the east
333 side of the col (blue dashed lines in Fig. 5B) clearly outline a glacier margin. The lithology
334 indicates that they were supplied by the En Garcia catchment. Their altitude on the slope
335 shows that the ice was thick enough to have joined the trunk glacier also fed by the three
336 other catchments on the south side of Puymorens. Other gneiss boulders located higher up
337 the same eastern mountain side (up to 2110 m; brown stars in Fig. 5B) outline the former
338 presence of a wider and thicker glacier, with limits probably very close (or identical) to those
339 of the LLGM. Note that the LLGM is not marked out by an abundance of ice-marginal
340 deposits because the col, at the time, was located within the accumulation rather than the
341 ablation zone of the trunk glacier (local ELA at the time of the LLGM: ~1800 m; Calvet et al.,
342 2004; Fig. 2C). Below the alignments of gneiss boulders, two well-preserved moraines (1930
343 m), exclusively consisting of granite boulders, outline the left margin of a glacier previously
344 fed by ice supplied by the Orri, Baladrar or Pas-de-la-Casa catchments, but already
345 disconnected from the En Garcia (Fig. 5B).
346 On the south side of Puymorens, a lateral moraine at the outlet of the Estanyol
347 subcatchment marks out the left margin of a glacier joining the Querol valley. Further west,
348 the Vinyole moraine complex (multiple ridges; green lines in Fig. 5B), is the combined
349 product of left-margin lateral moraines from a glacier exiting the Orri, and right-margin
350 moraines from another glacier fed by the Baladrar and Pas-de-la-Casa subcatchments (Fig.
351 3E). The lower right-margin moraine documents a time when the col was partially
352 deglaciated and hosted an ice-marginal lake now completely filled with sediment. On the left
353 side of Orri valley, the multiple lateral moraines of the Vinyole complex document

354 respectively (i) a 7-km-long glacier descending to elevations of 1650–1700 m (ice front); (ii) a
355 thinner and shorter (5 km) glacier reaching an elevation of 1900 m; and (iii) an even thinner
356 and shorter (3 km) glacier confined to the eastern part of the Orri cirque floor, below the
357 higher headwall of the catchment, and terminating at the 2100 m elevation contour.
358 Thereafter, the catchment hosted two rock glaciers: the older one developed at the time of
359 the 2100 m Orri glacial stillstand, the younger one formed after the glacier had retreated to
360 the cirque headwall and vanished.

361 Finally, the Baladrar and Pas-de-la-Casa subcatchments host a similar sequence of
362 rock glaciers and ice-margin deposits assignable to four substantially different ice extents
363 (Fig. 5B):

364 (i) The most elevated ribbon of ice-marginal debris occurs at 2280 m on the right side
365 of Pas-de-la-Casa valley (brown stars in Fig. 5B); it delineates a glacier boundary close
366 to that of the LLGM.

367 (ii) Further down the mountain side, several lateral moraines and a kame terrace
368 occurring at 2040 m mark out the right side of a substantially thinner and narrower
369 glacier. At this time, however, the thickness of the Ariège trunk glacier was still
370 sufficient to ensure a connection with the Baladrar tributary and reach the right-
371 margin lateral moraines of the Vinyole complex (Fig. 5B; green lines).

372 (iii) Further still down the hillsides, several lateral moraines located ca. 1980 m mark
373 out the right side of a former glacier confined to the Pas-de-la-Casa subcatchment.
374 The Ariège trunk glacier was still connected to its Baladrar tributary, and was
375 producing the frontal moraines mapped around 1580 m, 2 km upstream of
376 L'Hospitalet (red lines in Fig. 5B).

(iv) A last recessional stillstand, confined to the most elevated cirque floors and followed by a period of rock-glacier development, is identifiable in the Baladrar and Pas-de-la-Casa catchments (yellow lines in Fig. 5B).

4.1.2. Four glacial stades and their chronology

The sequence of ice-marginal deposits described above allows a succession of four stadial boundaries to be distinguished in the upper Ariège catchment.

(i) Glacier boundaries for the Petches/Ax-les-Thermes stadial are defined by the Petches lateral moraines. At this time, the trunk glacier in the upper part of the catchment was 100 to 150 m thinner than at the time of the LLGM (Fig. 6A). Ice was nonetheless thick enough to allow the tributaries (En Garcia, Orri, Baladrar and Pas-de-la-Casa) to join up as a unique composite glacier spilling north and south into the Ariège and Querol valleys, respectively. Col de Puymorens was thus still functioning at the time as a diffluence col.

(ii) Thereafter, the Ariège glacier retreated to a new position defined by the Mérens frontal moraines. In the upper part of the catchment, this interval produced the lower right-margin moraine of the Vinyole complex, which documents a partial deglaciation of the Puymorens pass, and the ice-margin deposits at 2040 m on the right side of the Pas-de-la Casa glacier (Fig. 6B).

(iii) At the time of the Hospitalet stillstand, the Ariège glacier was confined to its Pas-de-la-Casa subcatchment (Fig. 6C).

(iv) The last glacial stillstand recorded in the study area, before rock-glacier development in periglacial and/or paraglacial environments, corresponds to small cirque glaciers (less than 1 km long, Fig. 6D).

Tables 1 and 2 present the series of 22 new ^{10}Be surface exposure ages from boulders from nine sampling sites relevant to the Ax and Mérens glacial stillstands defined above. A tenth sampling site is located close to the LLGM ice limit near Puymorens. Overall, age results around Puymorens for sites A, C, D, F, G and H are often statistically indistinguishable, but age differences between sites are consistent with their relative positions in the landform sequence, and thus with the expected ice-recession chronology outlined above (Figs. 5–7). For example, boulders located on the most elevated right-marginal ribbon of glacial debris ca. 2280 m in Pas-de-la-Casa valley (Fig. 5B: site A) provide two consistent ages of 20.5±1.0 ka and 19.8±1.0 ka. On that basis, ice thickness at Puymorens at the end of the LGM (~20 ka) was almost identical to ice thickness during the LLGM. This is consistent with the ages of 18.0±1.0 ka and 18.6±1.2 ka obtained from site C (Fig. 5B, Table 2). Given that those boulders occur below the ribbon of gneiss boulders (1950 and 1980 m) on the NE side of the col (blue dashed lines, Fig. 5B), configurations of ice extent inferred from the geomorphological map dictate that the boulders at site C (100 to 150 m below the LLGM deposits around Col de Puymorens) match the Ax/Petches stadial boundaries rather than any other. On the same basis, the granite boulders from site D provide two ages of 17.8±1.2 and 18.2±1.0 (Fig. 5B; Table 2), thereby showing that the higher Vinyole moraines at the time of the Ax/Petches stillstand were medial moraines between the coalescing glaciers originating from the Orri and Baladrar catchments (Fig. 6A).

Boulders at site F1 provide more scattered results (17.9±0.9 ka on PUY03) and large uncertainty around PUY04 (16.5±2.4 ka), whereas boulders at site F2, on the right side of the Ariège glacier at the time of the Mérens stade (by which time the Puymorens col area was ice-free), provide ages of 15.7±1.1 ka and 16.5±1.2 ka (Fig. 5A; Table 2). Results for F2 are in good agreement (i) with the age of 16.8±1.6 ka and 15.8±1.6 from two other boulders embedded in the Estagnol left-margin moraine (site G; the third age for site G, 17.2±5.3 ka, has been removed because analytical error exceeds 15 %); and likewise (ii) with the 17.3±0.9 ka and 16.6±0.8 ka ages for the right-marginal moraine at 2040 m in Pas-de-la-Casa valley (site H; Fig. 5B, Table 2).

Results obtained at sites B and E are substantially more scattered (Fig. 5A; Table 2). Given the consistent ^{10}Be ages obtained in the vicinity of Puymorens (see above), we infer that: (i) the ages for PET10 (18.5±1.5 ka), PET11 (17.0±1.8 ka) and MER18 (15.5±1.2 ka) accurately estimate the time at which the Petches and Mérens lateral moraines were constructed; (ii) the ages for PET12 (20.7±1.7 ka) and MER19 (20.4±1.3 ka) are anomalously old (the likely cause being that boulders from the LLGM deposit situated on the hillside above sites B and E have polluted the Petches and Mérens moraines that occur lower down); (iii) the ages for PET09 (15.1±1.2 ka) and PET13 (15.7±1.4 ka) are too young given their low elevation (<1200 m). This lower part of the valley was engulfed from the early Holocene onward by a rapid return of temperate deciduous forest (Jalut et al., 1992), wherein the humid climate typical of forest habitats in the Pyrenean foothills would have ensured high rates of post-depositional weathering of the glacial deposits, thus making till-embedded boulders vulnerable to exposure-age anomalies.

Further TCN results from near Ax-les-Thermes and from Col de Puymorens, previously published by Delmas et al. (2011) and Pallàs et al. (2010) and recalibrated in the context of this study (see Suppl. Table 3.1), are of little direct use to the purpose of paleoclimate modelling or refining the chronology presented above. However, of crucial value for completing the LGIT history, four ^{10}Be ages were obtained by Pallàs et al. (2010) from boulders from the lateral moraine that marks out the smaller (3-km-long) and thinner (90 to 40 m) Orri glacier (terminal position: 2100 m). The exposure ages for LOR01 (14.4ka±1.4 ka), LOR03 (15.0±1.5 ka), LOR04 (13.7±1.0 ka), and LOR05 (15.4±1.9 ka), updated here on the basis of the recalibrations described in Section 3.2, provide a weighted mean age of 14.5±0.6 ka (Figs. 5B, 6D, 7, Table 3). This ascribes these glacier-margin deposits to the beginning of GI-1. On that basis, the rock glacier at the foot of the cirque headwall likely formed during GS-1, suggesting that the Orri glacier, despite being hosted by a north-facing cirque, had become extinct by the end of GI-1.

To summarize, the glacier stillstand chronology in the upper Ariège catchment (Fig. 7, Table 3) based on weighted mean ^{10}Be exposure ages is as follows: the (i) Pas-de-la-Casa (ribbon of ice-marginal boulders at 2280 m; 2 samples; weighted mean: 20.2±0.3 ka), (ii) Petches/Ax-les-Thermes (various ice-margin deposits: 6 samples; weighted mean of 18.0±0.5 ka), (iii) Mérens (various ice-margin deposits: 7 samples; weighted mean: 16.5±0.5 ka), and (iv) Orri (4 samples; weighted mean: 14.5±0.6 ka) stillstands span the latest LGM and most of the LGIT (early GS-2.1b, late GS-2.1b, GS-2.1a, and GI-1, respectively). The Hospitalet stillstand, situated between Mérens and Orri, is unsatisfactorily dated, but can still undergo glaciological and paleoclimatic modeling.

4.1.3 Glaciological and paleoclimatic reconstructions

On the basis of the successive ice boundaries presented and dated, the Harper and Humphrey application further allows the paleoglaciological (ELA, MBG) and paleoclimatic (ΔP and ΔT) conditions relating to each glacial stade to be reconstructed (Table 3; Figs. 6, 8). Ice-thickness profiles obtained for the Ax/Petches stade on the basis of Figure 6A yielded an ELA at 2012 m and a mass-balance gradient of 0.47±0.05 $m \cdot yr^{-1} \cdot 100\ m^{-1}$, and best-fitting P and T pairs of –62±8 % for paleoprecipitation relative to present-day reference conditions, and –9.7±0.5 °C for paleotemperature (Figs. 4C, 8). On the same basis, the best-fitting paleoclimatic conditions valid for the three subsequent glacial stades in the upper Ariège catchment are summarized and illustrated in Figures 6 and 8.

This, at the time of the Mérens stade, the Ariège glacier was about 15 km-long, 270 m thick (right-margin lateral moraine of Pas-de-la-Casa at 2040 m) and 300 m thick a few kilometres downsteam, at the Vinyole complex. Reconstructed glaciological and paleoclimatic conditions shown in Figure 8 are based on ice profile constraints set by these two points.

At the time of the Hospitalet stade, the Ariège glacier was 9.5 km long, the ice front stood at an elevation of 1580 m and formed on its right margin the lateral moraines located between 1870 and 2030 m. Paleoclimatic conditions shown in Figure 8 are based on ice thickness constraints (~100 m) set by these lateral moraines.

Constraints on ice thickness during that final period of residual cirque glaciers are provided by a lateral moraine in the Orri valley (ice thickness: 70–35 m, and ice front at 2100 m). Reconstructed paleoclimatic conditions based on that evidence are shown in Figure 8.

4.2. LGIT ice fluctuations and paleoclimate reconstructions among other east-Pyrenean catchments

Here we extend the methodology presented above as a pilot for the Ariège to other east-Pyrenean catchments where LGIT glacial chronologies have previously been documented (Table 3, Figs. 9–11). These include catchments within massifs to the north (Suc, Escale, Picot and Médecourbe) and south (Aránser, Malniu, Grave) of the Axial Zone (Fig. 2C). Chronological results are based on a recalibration of the population of existing TCN exposure ages for those valleys in order to update the age determination of the glacial landform sequences already mapped and dated in those catchments (see Suppl. Tables 3.2 and 3.3). Ice-marginal deposits ascribed to each local glacial stade allow paleoglaciological (ELA, MBG) and paleoclimatic (ΔP and ΔT) conditions to be reconstructed for several key locations that sample the climatic variability within the eastern Pyrenees (Fig. 2) and at different times of the LGIT (Table 3).

4.2.1. North side of the eastern Pyrenees

4.2.1.1. Suc valley (Trois-Seigneurs massif; after Delmas et al., 2011)

The Suc is a tributary of the Vicdessos River, on the south side of the Trois-Seigneurs massif. Four ^{10}Be ages from glacier-polished surfaces sampled at Freychinède bedrock step (site L, Fig. 9C) indicate that this bedrock exposure was ice-free ca. 16.1±1.0 ka (see also Suppl. Table 3.2). This, and an independent study by Jalut et al. (1982) based on radiocarbon dating and other lithostratigraphic criteria from a glacial paleolake, indicates that the Suc glacier was confined to its upper valley by the end of GS-2.1a. Glacier thickness, however, remains

511 imprecisely defined. Given its position 100 m above the valley floor and in a sheltered zone
512 (edge of a diffluent ice flow; Fig. 9C), the scenario constructed around site L only provides a
513 minimum value for glacier thickness. The available evidence is thus not an optimal input for
514 the glaciological model and for reconstructing paleoclimatic conditions in Suc valley at the
515 time of GS-2.1a (Fig. 10).
516
517 *4.2.1.2. Escale valley (Bassiès massif; after Crest et al., 2017)*
518
519 In a catchment just 4 km to the south of Suc valley (Fig. 2C), the presence of a frontal
520 moraine (1500 m) on the north side of the Légunabens diffluence col provides a proxy for
521 reconstructing a 6.5-km-long glacier in Escale valley, 150 m thick at the col (Fig. 9A). The ELA,
522 MBG, ΔP and ΔT best-fitting values produced on that basis are summarized in Table 3 and
523 Figure 10. Two ^{10}Be ages (BA15, BA16) provided a weighted mean of 16.1±0.2 ka (Fig. 9A,
524 Suppl. Table 3.2), thereby situating the Légunabens glacial stillstand within GS-2.1a. Further
525 upvalley, a smaller glacier marked out by a multiplicity of closely-spaced lateral moraines ca.
526 1885 m (Mouscadous local stade; weighted mean ^{10}Be ages from BA17 and BA18: 12.3±0.2
527 ka; Fig. 9B, Suppl. Table 3.2) place this stadial unit in GS-1.
528
529 *4.2.1.3. Picot and Médecourbe valleys (Soulcem catchment; Mont Calm–Pique d'Estats*
530 *massif; Jomelli et al., 2020)*
531
532 This area is situated in the upper part of the Vicdessos River catchment (Fig. 2C), 10–15 km
533 southeast of Légunabens. Picot is a steep-walled amphitheatre floored by three glacial

534 hollows, each containing a lake and separated from the other by ~100-m-high, subvertical
535 rock spurs bearing large, east-facing rock glaciers. Revised age values (inclusive of snow
536 shielding corrections) from the Outer Picot stadial moraine (elevation: 2060 m) provide a
537 weighted mean age of 17.8±0.3 ka (Picot-21, Picot-22, Fig. 9E; Suppl. Table 3.2). Deposits
538 associated with the Inner Picot glacial stillstand (ice front around 2200 m, Fig. 9F; Picot-17:
539 16.8±0.8 ka, Picot-18: 16.7±0.8 ka) and two glacially-polished bedrock surfaces at 2300 m
540 (Picot-15, Picot-16: weighted mean age of 16.7±0.1 ka; Suppl. Table. 3.2) overall place the
541 Outer and Inner Picot stadial deposits within GS-2.1b and GS-2.1a, respectively.
542 The small Médecourbe catchment (5 km south of Picot) also hosts a succession of five frontal
543 moraines located between 2200 and 2300 m and spanning a few hundred metres. Age
544 remodeling (inclusive of snow shielding) of nine samples produced slightly older exposure
545 ages than previously obtained by Jomelli et al. (2020)(Suppl. Table. 3.2) but, as in the Picot
546 catchment, the corrected ages do not fundamentally change the chronological
547 interpretations initially inferred. A weighted mean age of 13.2±0.9 ka (Med 1, Med 2, Med 3,
548 Med 4; Fig. 9D, Suppl. Table. 3.2) places the frontal moraines (elevation: 2200 m) at the
549 transition between GI-1 and GS-1. Given, however, the uncertainty both in snow-cover
550 duration and snow thickness at high altitudes, we assume that the Médecourbe glacial
551 stillstand occurred at the time of GS-1 rather than at the end of interstadial GI-1.
552
553 ***4.2.2. South side of the eastern Pyrenees***
554
555 *4.2.2.1. Aränser valley (Tossa Plana massif; after Palacios et al., 2015b; Andrés et al., 2018)*
556

557 At the time of the LLGM, the Aránser catchment in northern Spain hosted a 5–6-km-long
558 composite glacier on the south-eastern side of the flat-topped Tossa Plana (2600–2700 m,
559 border with Andorra). Restricting ^{36}Cl age recalculations to samples that were not
560 considered anomalous outliers by Palacios et al., (2015b) and Andrés et al. (2018), results for
561 PIR11-08, PIR11-09 and PIR11-12 provide a weighted mean age of 13.6±0.9 ka for the
562 Perafita moraines (Fig. 11A). On that basis, we infer that (i) the left-margin lateral moraines
563 of Perafita glacier were constructed during GS-2.1a; (ii) as in the case of the Orri catchment
564 on the north side of the orogen, the Perafita glacier became extinct during the GI-1
565 interstadial despite the benefits of the Tossa plateau acting as a (small) reservoir of
566 windblown snow feeding the SE-facing cirques. The catchment thereafter hosted active rock
567 glaciers (Palacios et al., 2015b).
568
569 *4.2.2.2. Malniu valley (Campcardós massif; Pallàs et al., 2010; Palacios et al., 2015b; Andrés*
570 *et al., 2018)*
571
572 The Campcardós massif (2914 m; Fig. 2), ~15 km east of Aránser, is also flat-topped and
573 favours snow accumulation downwind of northwesterly airstreams. In Malniu valley, the 24
574 revised exposure ages document four distinct Late Pleistocene stadial positions: (i) a MIS 3
575 and/or MIS 4 terminal moraine; (ii) a LGM frontal moraine situated inboard of, but very close
576 to, its MIS 3/ MIS 4 predecessor; (iii) a smaller, early GS-2.1b moraine (still at the time a
577 valley glacier fed by ice originating from the four south-facing glacial cirques; Fig. 11B); and
578 (iv) a GS-2.1a stadial moraine. Two rock glaciers developed subsequently during GI-1, both
579 confined to the glacial cirques. Revised model ages from the six boulders sampled on the

580 lateral moraines provide a weighted mean age of 19.2±0.7 ka (PIR13-09, PIR13-10, OMA01
581 to OMA04, Suppl. Table 3.3), which confirms that these stadial deposits belong to GS-2.1b.
582 The glaciological and paleoclimatic reconstructions are based on the frontal and lateral
583 moraines ascribed to GS-2.1b: ice thickness was ~50 m close to ^{10}Be sample OMA, and ~80 m
584 close to ^{36}Cl sample PIR13-09/10 (see Fig. 11B).
585
586 *4.2.2.3. Upper Têt, or Grave, valley (Carlit massif; after Delmas, 2005; Delmas et al., 2008;*
587 *Crest et al., 2017; Tomkins et al., 2018)*
588
589 The Grave valley is located 25 km NE of Campcardós. Although south facing and relatively
590 dry, the valley receives northwesterly airflow and precipitation through a saddle in the
591 headwall. Radiocarbon ages obtained from a peatbog (2150 m) on the valley floor suggest
592 early and rapid post-LLGM glacial recession, with ice becoming mostly confined to cirque
593 floors at the end of the LGM. A SHED age of 16.1±0.5 ka on a left-margin lateral moraine
594 (elevation: 2200–2100 m; Tomkins et al., 2018) nonetheless hints at an ice front located
595 around 2020 m in the Grave valley at that time, and thus accrediting the possibility that the
596 peatbog was overridden by a readvancing glacier during GS-2.1a (Fig. 11C). Based on that
597 scenario, the reconstructed 3-D ice surface at the time of GS-2.1a shows a glacier 6.5 km
598 long and thinning in stages from 130 to 25 m in the ablation zone. On the basis of the ice-
599 thickness profile constrained by the left-margin lateral moraine, the paleoclimatic model
600 parameters are summarized in Table 3 and Figure 11D. In the uppermost part of the
601 catchment, several frontal and lateral moraines mark out two smaller (and younger) glacier
602 stillstands, with their respective ice fronts reaching 2150 and 2160 m. Revised model ages

603 for both these local stades provide weighted means of 13.8±0.6 ka (ice front at 2150 m, sites
604 M) and 13.1±0.6 ka (ice front at 2160 m, site N and O), respectively (Suppl. Table 3.3). Such
605 an age sequence places the two events within the GI-1 interstadial (Fig. 11E).
606
607 **5. Discussion**
608
609 Based on paleoglaciological (ELA, MBG) and paleoclimatic (ΔP, ΔT) results acquired from the
610 glacial stillstands documented above (Section 4, Table 3 and Fig. 12), we analyse patterns of
611 LGIT climatic conditions in the eastern Pyrenees (Section 5.1) and discuss their implications
612 for atmospheric circulation in a wider European context (Section 5.2).
613
614 **5.1. LGIT glacier fluctuations as proxies for east-Pyrenean climate variability through space**
615 **and time**
616
617 As emphasized in Section 3.3, in mountain settings where modern climatic (MMT, CMP,
618 altitudinal lapse rates) and glaciological (*DDF*) constraints are unavailable, such as in many
619 parts of the Pyrenees, model reconstructions of paleoclimate can only be addressed in
620 relative terms, i.e., by comparing (i) simultaneous conditions in different parts of the
621 mountain range during a particular time interval; or (ii) relative P and T changes over a given
622 chronological sequence in different valleys. Results reported in Table 3 document a sharp
623 climatic contrast between the north and the south side of the range from the end of the GS-
624 2.1b (Section 5.1.1). They also highlight a clear transformation of regional climate during the

LGIT (Section 5.1.2), with a significant increase of temperatures and precipitation between GS-2.1a and GI-1. Impacts of GS-1-related cooling (Younger Dryas) are also examined.

5.1.1. A clear and enduring north–south climatic divide during GS-2.1b and thereafter

In terms of glacier size, the upper Ariège valley hosted the largest: 27.5 km at the time of GS-2.1b (Ax stade), and still 19.5 km during GS-2.1a (Mérens stade). Coeval glaciers on the south-facing sides of the Campcardós (GS-2.1b, Malniu) and Tossa Plana (GS-2.1a, Aránser) were just 2–3 km long, and a little longer (~6 km) on the south-facing sides of the Carlit (GS-2.1a Grave) and Bassiès massifs (GS-2.1a, Légunabens). These size contrasts are mostly explained by glacial catchment hypsometry (specifically: the surface area of catchments situated above ELA), which controls the volume of ice in the accumulation zone (Suppl. Material 4). With 90.7 km^2 at the time of GS-2.1b, and still 25.3 km^2 during GS-2.1a, the upper Ariège afforded by far the best conditions during the early LGIT compared to <4.4 km^2 in the other massifs during the same period (Table 3). Position of the ELA and mass-balance gradient are direct indicators of montane paleoclimate because they integrate information about the regional climate and about local (topoclimatic) effects. On that basis, the glaciological modeling results document colder and wetter conditions among the northern massifs of the study area, with:

(i) systematically lower ELAs on the north side of the range (during GS-2.1b: respectively 2012 m and 2413 m for the Ax and Malniu stillstands; during GS-2.1a: respectively 2152 m and 2473 m for the Mérens and Aránser stillstands);

(ii) systematically higher mass-balance gradients, i.e., wetter conditions, on the north side of the range (GS-2.1b: respectively 0.47±0.05 and 0.37±0.06 $m \cdot yr^{-1} \cdot 100\ m^{-1}$ for

Ax and Malniu; GS-2.1a: respectively 0.50±0.05 and 0.35±0.05 m·yr^{-1}·100 m^{-1} for Mérens and Aránser; Fig. 12, Table 3).

As explained in Section 3.3, ΔT and ΔP values reported in Table 3 should be analyzed in relative terms, i.e., whether contrasts between massifs in the past were similar, larger or smaller than today's. The data indicate that north–south climatic contrasts were more pronounced during the early LGIT (GS-2.1b and GS-2.1a) than they are today. At the time of GS-2.1b, this pattern is particularly clear in the case of temperatures (–9.7±0.5 °C vs. –7.5±0.5 °C during the Petches/Ax and Malniu stillstands). At the time of GS-2.1a, the pattern mainly concerned precipitation (–44±11 % vs. –77±7 % during the Mérens and Aránser stades).

Nested within this north–south divide, some finer spatial distinctions are apparent for GS-2.1a (Fig. 12, Table 3). Among the south-facing catchments, the Grave stillstand (ELA: 2383 m, MBG: 0.40±0.04 m·yr^{-1}·100 m^{-1}) occurred in a cooler and wetter environment than the Aránser further west (ELA: 2473 m, MBG: 0.35±0.05 m·yr^{-1}·100 m^{-1}). Among the northern massifs, the Légunabens stillstand (ELA: 2012 m, MBG: 0.44±0.05 m·yr^{-1}·100 m^{-1}) occurred in a cooler and drier environment than further east (Mérens stillstand in the upper Ariège valley; ELA: 2152 m, MBG: 0.50±0.05 m·yr^{-1}·100 m^{-1}). It is remarkable that the model data are sufficiently sensitive to evidence subsidiary topoclimatic effects of this kind: the NW–SE Grave valley head coincides with a saddle in the ridgetop, allowing the accumulation zone to be directly supplied by Atlantic airflow from the NW. The Vicdessos valley, in contrast, strikes NE–SW and is sheltered from northwesterly airflow by high summits. Also revealed by the data is the steeply declining precipitation gradient along the Vicdessos valley between the Trois-Seigneurs massif, which stands in a front-line position vulnerable to

671 Atlantic weather systems, and the inner Bassiès and Mont Calm massifs, which stand in more
672 sheltered interior positions (Fig. 2). The gradient is perceptible in the data for GS2.1a (ΔP:
673 +45±25 % at Freychinède, –45±11 % at Légunabens, –80±5 % at Inner Picot) and for GS-1 (–
674 21±16 % at Mouscadous, –60±7 % at Médecourbe).
675
676 ***5.1.2 Evidence of climatic change over time and compatibility with records for SW Europe***
677
678 The data in Table 3 show a change in climatic conditions from GS-2.1a to GI-1. In the
679 upper Ariège valley, temperatures rose by +2.5±0.5 °C between the Mérens and Orri stadial
680 units (GS-2.1a: –8.1±0.5 °C; GI-1: –5.6±0.5 °C), and a slight increase in precipitation (+ 20±16
681 %) can be inferred for the same time interval (GS-2.1a: –44±11 %; GI-1: –24±16 %). The
682 climatic downturn (GS-1) cannot be directly documented in the upper Ariège valley because
683 dated glacial deposits are unavailable. Two other sites (Mouscadous and Médecourbe) fail to
684 provide clear trends because GI-1 is undocumented in the Vicdessos valley. Glacier
685 stillstands documented in the Bassiès massif (Légunabens and Mouscadous), however, show
686 that GS-1 was substantially warmer and a little wetter than the earlier stages of GS-2.1a
687 (2.1±0.5 °C warmer and ~24±16 % wetter, with an ELA 190 m higher up the mountain; Table
688 3). On that basis, and given further the ΔT and ΔP changes (+2.5±0.5 °C, and +20±16 %)
689 recorded between the Mérens and Orri glacial stillstands, it remains indirectly plausible that
690 small glacial cirques were present in the upper Ariège (Pas-de-la-Casa) during GS-1.
691 Acquiring ages brackets for the Hospitalet moraines downvalley and for cirque outlet
692 moraines further upvalley (Fig. 5B) would provide the missing evidence, but indirect
693 constraints can nonetheless be adduced by the recalculated ^{10}Be ages for the Orri frontal

694 moraine (2100 m). These show that the last time a glacier was hosted by this cirque was not
695 GS-1, as initially envisaged by Pallàs et al. (2010), but instead GI-1 (Table 3). This arises
696 because revised ^{10}Be dating protocols tends to generate systematically older exposure ages
697 than under previous calibrations, particularly when snow shielding is included (see Suppl.
698 Material 3). Exactly as on the south side of the range, cirque glaciers in this region of the
699 Axial Zone thus dwindled to extinction during GI-1. When applying to the south side of the
700 range the rises in ELA recorded in the upper Ariège (+271 m between GS-2.1a and GI-1) and
701 Bassiès (+191 m between GS-2.1a and GS-1), all the valley heads of the southern catchments
702 likewise underwent definitive deglaciation during the course of GI-1. The potential for ice
703 accumulation on Tossa Plana and Campcardós was insufficient for a subsequent readvance
704 during GS-1 (calculated ELA on the south side of those two massifs: 2740–2660 m). These
705 conclusions are consistent with the development of rock glaciers in the cirques of the
706 southern massifs during GI-1 and continuing into GS-1—most of this occurring in a
707 paraglacial context of strong slope response to glacier extinction (Delmas et al., 2008;
708 Andrés et al., 2018). The Grave valley in the Carlit massif may have continued to host small
709 glaciers, 1 to 2 km long, benefiting from windblown snow accumulation and local
710 topographic effects during GI-1 (see Section 4.2.2.3)—and probably also during GS-1, as
711 suggested by three ages (11.49 ± 1.8, 12.6 ± 1.5, 12.6 ± 2.7; Suppl. Table 3.3) from a glacially-
712 polished bedrock step located further back from the GI-1 moraine, ca. 2380 m.
713 Overall, climatic changes reported in this study concur with a very large array of
714 independently reported local and regional paleoenvrionmental proxies in the Pyrenees and
715 Iberia (Fig. 12). Pollen spectra documented from the lake sediments at Freychinède (1350
716 m), La Borde (1660 m), Ruisseau de Laurenti (1860 m), Balcère (1770 m), and La Moulinasse

717 (1360 m), for example (locations in Fig. 2C), confirm that climatic conditions in the inner
718 valleys of the eastern Pyrenees were substantially colder and drier during GS-2.1b and GS-
719 2.1a (particularly under Mediterranean influence) than during GI-1 (synthesis in Jalut et al.,
720 1992; Reille and Lowe, 1993; Reille and Andrieu, 1993). Further west, LGIT summer
721 paleotemperatures inferred from *Chironomidae* in the lacustrine sediment sequence of Ech
722 (710 m; central Pyrenees) and Laguna de la Roya (1608 m, NW Iberia) confirm the cold
723 conditions of GS-2.1b and GS-2.1a, followed by a rapid rise in temperature conditions during
724 GI-1 (Millet et al., 2012; Sobrino et al., 2012). The Ech and Laguna de la Roya lacustrine
725 sequences also capture the cooling event corresponding to GS-1. They were associated with
726 summer temperatures at least 2 °C higher than at the time of GS-2.1a (Millet et al., 2012;
727 Muñoz Sobrino et al., 2012). Moreover, the wetter conditions during GS-1 compared to GS-
728 2.1a are independently confirmed by the speleothem geochemistry of Seso cave (Central
729 Pyrenees, Spain; Bartolomé et al., 2015) and pollen-based climate reconstructions from the
730 Alborán Sea (Combourieu-Nebout et al., 2009; Rodrigo-Gámiz et al., 2011). Finally, multi-
731 proxy analysis of lacustrine (Fletcher et al., 2010; Rius et al., 2014; Moreno et al., 2012, 2014;
732 González-Sampériz et al., 2017; Oliva-Urcia et al., 2017) and marine (Combourieu-Nebout et
733 al., 2009; Dormoy et al., 2009; Melki et al., 2009; Naughton et al., 2019) sequences from
734 within the wider region of SW Europe indicate similar chronologies, all of these in step with
735 global records (Lisiecki and Raymo, 2005; Rasmussen et al., 2014; Lambeck et al., 2014).
736
737 **5.2 LGIT paleoclimates of the eastern Pyrenees in the wider European context**
738 Paleoclimatic conditions in the eastern Pyrenees, and their chronology and patterns
739 of change discussed in Section 5.1, extend the existing spectrum of evidence documenting

changes in atmospheric circulation across Europe during the transition from the LGM to the Holocene.

The trajectories over Europe of low-pressure weather systems initially generated in the North Atlantic during the Late Pleistocene were essentially controlled by shifts in latitude of the Polar Front Jet Stream (PFJS). The position of the PFJS is itself a function of land- and sea-temperature-related high-pressure centres generated by the expansion and recession of (i) the North American Ice Sheet, (ii) sea ice in the North Atlantic, and (iii) the Fennoscandian Ice Sheet, which block or deflect the band of Westerlies southward (Bakke et al., 2009; Hofer et al., 2012; Beghin et al., 2015; Merz et al., 2015).

During the LGM, displacement of the PFJS southward to ~38° N (see models by Merz et al., 2015) was conducive to cold winter air masses invading the Mediterranean Basin more frequently than under interglacial conditions such as today. In that context, low-pressure systems would track frequently through the Straits of Gibraltar and directly across the full fetch of the Mediterranean. They would also, however, funnel through the lowland region between the ice-capped Alps and Pyrenees and into the Gulf of Lion, Ligurian Sea and Tyrrhenian Sea (Florineth and Schlüchter, 2000; Kuhlemann et al., 2008), with the relatively warm surface waters of the Mediterranean all the while providing ideal conditions for fuelling moisture advection and generating cyclonic weather (Hayes et al., 2005). Under the dynamics promoted by this atmospheric configuration, valley glaciers hosted by mountains of the Mediterranean peninsulas, but also by the southern massifs of the Alps and Pyrenees, found conditions for expansion (Haerberli and Penz, 1985; Florineth and Schlüchter, 2000; Kuhlemann et al., 2008; Delmas et al., 2011; Luetscher et al., 2015; Ludwig et al., 2016; Monegato et al., 2017).

After the LGM, insolation increased (Fig. 12) and the North American Ice Sheet began to recede during GS-2.1a (Stokes et al., 2012; Monegato et al., 2017). This triggered a displacement of the PFJS northward to latitudes of ~40–42° N between 18.3 and 15.9 ka (Eynaud et al., 2009), thus reducing the effects of southerly storm tracks and entailing glacier recession in the circum-Mediterranean mountain ranges. In the eastern Pyrenees, this is confirmed by the concomitant rise of ELAs from ~1800 m to ~2050–2150 m in northern massifs and from ~2200 m to ~2380–2450 m among their southern counterparts (Fig. 12). Magnitudes of change in temperature and precipitation between the LGM and early LGIT remain unknown but, whether on the north or the south side of the range, paleoclimatic data from east-Pyrenean glaciers indicate overall a very cold and dry environment during GS-2.1b and GS-2.1a (Fig. 12).

This record concurs with trends documented Europe-wide. In the Austrian Alps, the Gschnitz stadial ELA (~16–17 ka, i.e., GS-2.1a) was 1930 m, and paleotemperatures and paleoprecipitations were respectively 10 °C and 70 % lower than today (Ivy-Ochs et al., 2006). In the Tatra Mountains, the ELA was 1600–1800 m, and paleotemperatures and paleoprecipitation were respectively 9–10 °C and 30–50 % lower than today (Makos et al., 2018). In the Cantabrian Mountains (Fuentes Carrionas), the ELA was ~1990 m at a time when paleotemperatures and paleoprecipitation were respectively 10.4 °C and 30 % lower than today (Pellitero et al., 2019). The eastern Mediterranean area was comparatively more humid (Mount Erciyes, in central Turkey, recorded paleoprecipitation 50 % higher than today and paleotemperatures lower by 4.5–6.4 °C; Sarikaya et al., 2009), still probably benefiting from intense convection over the Levantine Sea with its warmer SSTs coming into contact with cold winter air (Fig. 12; Castañeda et al., 2010).

The study area nonetheless also records a contrast in paleoprecipitation totals between the northern and southern massifs during GS-2.1a (Fig. 12), highlighting more abundant supply of precipitation from Atlantic sources and supplying glaciers in the northern massifs. The N–S contrast points to a climatic regime with a PFJS now roughly positioned at Pyrenean latitudes, with snowfall generated by low-pressure weather systems over the North Atlantic impacting the northern Pyrenees more strongly than during the LGM, and masses of cold air and their associated cold fronts periodically pinching off the polar hemisphere and getting funneled southeastward across France to the western Mediterranean. The funneling scenario is supported by the age of OSL-dated eolian deposits in the lower Rhône valley, which document wind acceleration from the north and northwest between 27 and 16 ka, i.e., during the LGM and onward through to GS-2.1a (Bosq et al., 2018). Adding to the continuing outflow of glacial waters from the Rhône catchment, cooler SSTs over the Gulf of Lion, generated by these frequent and intense northerly (mistral) and northwesterly (tramontane) winds, also entailed strong upwelling effects (Melki et al., 2009). These cumulative factors overall curbed the potential for convective circulation above the western Mediterranean, and mostly shut down opportunities (which were prevalent during the LGM) for heavy snowfall over the southern massifs of the eastern Pyrenees during GS-2.1a.

General climatic conditions became milder during GS-1 compared to GS-2.1a, and involved a rise in ELAs and in T and P values throughout Europe. In the High Tatra Mts., the reconstructed GS-1 ELA (12.5 ka) had risen to 1950–2000 m, and T and P were respectively 6 °C and 15–25 % lower than today (Makos et al., 2012, 2018). In the Western Alps, during the transition between GS-1 and the earliest Holocene (~11 ka), the ELA of the Argentière glacier

(Mont Blanc) was ~2400 m, with T and P respectively 3.6–5.5 °C and 0–45 % lower than today, (Protin et al., 2019). In the Cantabrian Mountains (Fuentes Carrionas), the GS-1 ELA (12.4 ka) was 2265 m, ΔT was –9 °C, but ΔP only –2 % (Pellitero et al., 2019). As shown in Figure 12, ELAs in the eastern Pyrenees had risen everywhere to at least 2200 m, often to 2500 m, thus reducing potential glacier accumulation zones to vanishingly small sizes given the hypsometry of the massifs (Suppl. Material 4).

A study of Europe-wide paleoprecipitation based on 122 reconstructed glacier boundaries and proxy atmospheric temperatures has allowed precipitation anomalies during GS-1 to be simulated widely across Europe (Rea et al., 2020). With greater precision than for GS-2.1, the results for GS-1 show a strong contrast between negative and positive P anomalies in the western and eastern Mediterranean, respectively. These are fully consistent with the Pyrenean results presented here, which indicate, however, a slightly more negative precipitation anomaly (–20 %) than adduced by Rea et al. (2020). This minor difference can be explained by the fact that Rea et al. (2020) based their evidence in the eastern Pyrenees on 4 data points (from the Carlit, Campcardós and Puymorens areas), all of which overestimate the size of glaciers during GS-1 because the arithmetics of age recalibration (this study) make those stadial positions effectively older (GI-1) than GS-1. Additionally, Rea et al. (2020) did not integrate finer-scale orographic effects, whereas model calibration on modern glaciers in this study provides tighter controls on the local impact of orographic effects on precipitation values. The eastern Pyrenees at the time of GS-1 were thus even drier than made out by the Europe-wide model.

As a result of glaciers having largely reached extinction during GI-1, except in local situations where wind-blown snow accumulation and elevated catchments appears to have

832 extended the life of cirque glaciers into the Younger Dryas (these two exceptions are the
833 Mont Calm and Bassiès massifs), data from the eastern Pyrenees are ill-suited to
834 documenting climatic conditions during the Younger Dryas. Based on their Europe-wide
835 database, Rea et al. (2020) have nonetheless shown that, despite the PFJS having by that
836 time relocated to 54–55°N and favored a return to Westerlies-dominated circulation,
837 outbreaks of cold northerly air entering the Mediterranean Basin were still commonly
838 occurring. These cold air masses, however, were interacting with the higher SSTs of the
839 eastern Mediterranean more forcefully than with the cooler SSTs of the western
840 Mediterranean, thereby maintaining the dry climate detected by this study as early as GS-
841 2.1a among the southern massifs of the Pyrenees. Cold and dry conditions in the eastern
842 Pyrenees during the Younger Dryas are fully compatible with the widespread presence of
843 rock glaciers (and an active permafrost layer) among the cirques that had been vacated
844 during GI-1 by the last remaining glaciers. Full dominance of the Westerlies similar to the
845 interglacial conditions of today only became established after the GS-1-to-Holocene
846 transition, when global insolation had risen sufficiently to definitively melt large volumes of
847 North American Ice Sheet, Fennoscandian Ice Sheet and North Atlantic sea ice (Fig. 12;
848 Stokes et al., 2012; Hughes et al., 2015; Maffezzoli et al., 2019), consequently displacing the
849 PFJS to latitudes of 58°N (Merz et al., 2015).
850
851 **6. Conclusions**
852 The last Glacial to Interglacial Transition period was a period during which receding outlet
853 glaciers fragmented into a large number of short, disconnected cirque or valley glaciers.
854 Their mass balances increasingly became controlled by local topoclimatic conditions

855 potentially bearing limited relation to regional atmospheric drivers, but patterns across the
856 study area nonetheless document consistent trends and scenarios of regional importance, as
857 follows:

858 (i) New, and previously published but updated, cosmogenic exposure ages (n = 86)
859 reveal a LGIT deglaciation pattern across the eastern Pyrenees involving clearly
860 defined recessional standstills, or local stades, occurring during GS-2.1b, GS-2.1a and
861 GI-1. Residual cirque glaciers during GS-1 were present only in valleys characterized
862 by elevated accumulation zones and favorable topoclimatic conditions, and thus in a
863 very small minority.

864 (ii) When calculated on the basis of the most recent updates in TCN dating (Section 3.2),
865 ^{10}Be exposure ages from publications in the last 10 years tend to increase
866 systematically by 7–10 %, and by up to ~18 % when snow shielding corrections are
867 applied (Suppl. Material 3). The incidence of such calibrations on the construction of
868 paleoclimate chronologies is thus far from trivial.

869 (iii) Climate in the eastern Axial Zone of the Pyrenees was substantially colder and drier
870 during GS-2.1b and GS-2.1a than during GI-1 and, although with fewer constraints,
871 GS-1.

872 (iv) The pattern of ELAs and mass-balance gradients in the eastern Pyrenees reveals a
873 general N–S gradient during GS2.1b and GS2.1a, with lower ELAs and higher mass-
874 balance gradients among massifs on the north side of the range. This pattern
875 indicates wetter conditions on the north side. The N–S contrasts, which are still sharp
876 and prominent today (cooler and wetter north, Fig. 1) have thus been in place for at
877 least 19,000 years, i.e., since the end of the LGM.

(v) In a context dominated by more southerly storm tracks than at present because the Polar Front Jet Stream was positioned at latitudes of ~40–42°N between 18 and 16 ka, the eastern Pyrenees during the earlier part of the LGIT remained sheltered not just from Atlantic but also from Mediterranean weather systems. Thus, whereas polar air outbreaks along the Polar Front interacted with warmer SSTs in the eastern Mediterranean region, thereby promoting cyclonic weather and snowfall over the peninsulas, cold air met with comparatively cooler SSTs in the western Mediterranean (Fig. 12), overall suppressing abundant precipitation. As a result, the eastern Pyrenees remained comparatively dry despite their position as land bridge between the Atlantic and Mediterranean.

(vi) Full restoration of Westerlies-dominated circulation over Europe only occurred somewhat later (GS-1, i.e., Younger Dryas), after which time global warming, added to unsuitable catchment hypsometries, definitively counteracted possibilities for rebooting glacier expansion despite a return to Atlantic-influenced wetter conditions, including among the northern massifs of the Pyrenees.

Acknowledgments

TCN surface exposure dating was funded by the Bureau des Recherches Géologiques et Minières through the RGF AMI-Pyr programme. The ASTER AMS national facility (CEREGE, Aix-en-Provence) is supported by INSU/CNRS, IRD, and by the ANR through its 'Projets thématiques d'excellence' programme for the 'Equipements d'excellence' ASTER-CEREGE initiative. We thank Vincent Favier, Vincent Jomelli, and Pierre-Henri Blard, for their advice over the glaciological modeling, Pierre René and Pedrero Muñoz for sharing glaciological

901 data, and the Meteorological Service of Catalonia for sharing temperature and precipitation
902 data. Benjamin Chandler and Philip Hughes provided thorough and much appreciated
903 reviews of the manuscript.
904

905 **References**

906 Andrés, N., Gómez-Ortiz, A., Fernández-Fernández, J.M., Tanarro, L.M., Salvador-Franch, F.,
907 Oliva, M., Palacios, D., 2018. Timing of deglaciation and rock glacier origin in the
908 southeastern Pyrenees: a review and new data. Boreas 47, 1050–1071.

909 Arnold, M., Merchel, S., Bourlès, D.L., Braucher, R., Benedetti, L., Finkel, R.C., Aumaître, G.,
910 Gottdang, A., Klein, M., 2010. The French accelerator mass spectrometry facility ASTER:
911 improved performance and developments. Nuclear Instrumentation Methods in Physics
912 Research, Section B: Beam Interactions with Materials and Atoms 268, 1954–1959.

913 Bakke, J., Lie, O., Heegaard, E., Dokken, T., Haug, G.H., Birks, H.H., Dulski, P., Nilsen, T., 2009.
914 Rapid oceanic and atmospheric changes during the Younger Dryas cold period. Nature
915 Geoscience 2, 202-205.

916 Balco, G., Stone, J.O., Lifton, N.A., Dunai, T.J., 2008. A complete and easily accessible means
917 of calculating surface exposure ages or erosion rates from ^{10}Be and ^{26}Al measurements.
918 Quaternary Geochronology 3, 174–195.

919 Bartolomé, M., Moreno, A., Sancho, C., Stoll, H.M., Cacho, I., Spötl, C., Belmonte, Á.,
920 Edwards, R.L., Cheng, H., Hellstrom, J.C., 2015. Hydrological change in southern Europe
921 responding to increasing North Atlantic overturning during Greenland Stadial 1. Proceedings
922 of the National Academy of Sciences 112, 6568–6572.

923 Batalla, M., Ninyerola, M., Catalan J., 2018. Digital long-term topoclimate surfaces of the
924 Pyrenees mountain range for the period 1950–2012. Geoscience Data Journal 5, 50–62.
925 Beghin, P., Charbit, S., Dumas, C., Kageyama, M., Ritz, C., 2015. How might the North
926 American ice sheet influence the northwestern Eurasian climate? Climate of the Past 11,
927 1467-1490.
928 Biette, M., Jomelli, V., Favier, V., Chenet, M., Agosta, C., Fettweiss, X., Ho Tong Minh, D., Ose,
929 K., 2018. Estimation des températures au début du dernier millénaire dans l'ouest du
930 Groenland : résultats préliminaires issus de l'application d'un modèle glaciologique de type
931 degré jour sur le glacier Lyngmarksbræen. Géomorphologie 24, 31–41.
932 Blard, P.-H., Lavé, J., Pik, R., Wagnon, P., Bourlès, D., 2007. Persistence of full glacial
933 conditions in the central Pacific until 15,000 years ago. Nature 449, 591–594.
934 Bosq, M., Bertran, P., Degeai, J.P., Kreutzer, S., Queffelec, A., Moine, O., Morin, E., 2018. Last
935 Glacial aeolian landforms and deposits in the Rhône Valley (SE France): Spatial distribution
936 and grain-size characterization. Geomorphology 318, 250–269.
937 Braithwaite, R., Zhang, Y., 2000. Sensitivity of mass balance of five Swiss glaciers to
938 temperature changes assessed by tuning a degree-day model. Journal of Glaciology 46, 7–14.
939 Braucher, R., Merchel, S., Borgomano, J., Bourlès, D.L., 2011. Production of cosmogenic
940 radionuclides at great depth: a multi element approach. Earth and Planetary Science Letters
941 309, 1–9.
942 Braucher, R., Guillou, V., Bourlès, D.L., Arnold, M., Aumaître, G., Keddadouche, K., Nottoli, E.,
943 2015. Preparation of ASTER in-house $^{10}Be/^{9}Be$ standard solutions. Nuclear Instrumentation
944 Methods in Physics Research, Section B: Beam Interactions with Materials and Atoms 361,
945 335–340.

946 Cacho, I., Grimalt, J.O., Pelejero, C., Canals, M., Sierro, F.J., Flores, J.A., Shackleton, N., 1999.
947 Dansgaard-Oeschger and Heinrich event imprints in Alboran Sea paleotemperatures.
948 Paleoceanography 14, 698–705.
949 Cacho, I., Grimalt, J.O., Canals, M., Sbaffi, L., Shackleton, N.J., Schönfeld, J., Zahn, R., 2001.
950 Variability of the Western Mediterranean sea surface temperature during the last 25,000
951 years and its connection with the Northern Hemisphere climatic changes. Paleoceanography
952 16, 40–52.
953 Calvet, M., 2004. The Quaternary glaciation of the Pyrenees. In: Ehlers J., Gibbard P. (eds),
954 Quaternary Glaciations-Extent and Chronology, part I: Europe, Elsevier, 119–128.
955 Calvet, M., Delmas, M., Gunnell, Y., Braucher, R., Bourlès, D., 2011. Recent advances in
956 research on Quaternary glaciations in the Pyrenees. In: Ehlers, J., Gibbard, P.L., Hughes, P.
957 (eds), Quaternary Glaciations. Extent and Chronology, a closer look Part IV. Developments in
958 Quaternary Science 15, Elsevier, pp. 127–139.
959 Calvet, M., Gunnell, Y., Farines, B., 2015. Flat-topped mountain ranges: their global
960 distribution and value for understanding the evolution of mountain topography.
961 Geomorphology 241, 255-291.
962 Castañeda, I.S., Schefuß, E., Pätzold, J., Sinninghe Damsté, J.S., Weldeab, S., Schouten, S.,
963 2010. Millennial-scale sea surface temperature changes in the eastern Mediterranean (Nile
964 River Delta region) over the last 27,000 years. Paleoceanography 25, 1–13.
965 Chandler, B.M.P., Lovell, H., Boston, C.M., Lukas, S., Barr, I.D., Benediktsson, Í.Ö., Benn, D.I.,
966 Clark, C.D., Darvill, C.M., Evans, D.J.A., Ewertowski, M.W., Loibl, D., Margold, M., Otto, J.C.,
967 Roberts, D.H., Stokes, C.R., Storrar, R.D., Stroeven, A.P., 2018. Glacial geomorphological

968 mapping: A review of approaches and frameworks for best practice. Earth-Science Reviews
969 185, 806–846.
970 Chandler, B.M.P., Boston, C.M., Lukas, S., 2019. A spatially-restricted Younger Dryas plateau
971 icefield in the Gaick, Scotland: Reconstruction and palaeoclimatic implications. Quaternary
972 Science Reviews 211, 107–135.
973 Chmeleff, J., von Blanckenburg, F., Kossert, K., Jakob, D., 2010. Determination of the ^{10}Be
974 half-life by multicollector ICP–MS and liquid scintillation counting. Nuclear Instruments and
975 Methods in Physics Research. Section B: Beam Interactions with Materials and Atoms 268,
976 192–199.
977 Claude, A., Ivy-Ochs, S., Kober, F., Antognini, M., Salcher, B., Kubik, P.W., 2014. The Chironico
978 landslide (Valle Leventina, southern Swiss Alps): age and evolution. Swiss Journal of
979 Geosciences 107, 273–291.
980 Combourieu-Nebout, N., Peyron, O., Dormoy, I., Desprat, S., Beaudouin, C., Kotthoff, U.,
981 Marret, F. 2009. Rapid climatic variability in the west Mediterranean during the last 25,000
982 years from high resolution pollen data. Climate of the Past 5, 503–521.
983 Copons, R., Bordonau, J. 1996. El registro sedimentario del cuaternario reciente en el lago
984 Redó d'Aigües Tortes (Pirineos centrales). In: Grandal d'Anglade A., Pagés Valcarlos J., Eds.
985 IV° Reunión de Geomorfologia, Sociedad Española de Geomorfologia O Castro, 249–260.
986 Crest, Y., Delmas., M., Braucher., R., Gunnell., Y., M, Calvet, M., 2017. Cirques have growth
987 spurts during deglacial and interglacial periods: Evidence from ^{10}Be and ^{26}Al nuclide
988 inventories in the central and eastern Pyrenees. Geomorphology 278, 60–77.
989 Delmas, M., 2005. La déglaciation dans le massif du Carlit (Pyrénées orientales) : approches
990 géomorphologique et géochronologique nouvelles. Quaternaire 16, 45–55.

991 Delmas, M., 2015. The last maximum ice extent and subsequent deglaciation of the
992 Pyrenees: an overview of recent research. Cuadernos de Investigación Geográfica 41, 109–
993 137.
994 Delmas, M., Gunnell, Y., Braucher, R., Calvet, M., Bourlès, D. 2008. Exposure age chronology
995 of the last glacial cycle in the eastern Pyrenees. Quaternary Research 69, 231–241.
996 Delmas, M., Calvet, M., Gunnell, Y., Braucher, R., Bourlès, D., 2011. Palaeogeography and
997 ^{10}Be exposure-age chronology of Middle and Late Pleistocene glacier systems in the northern
998 Pyrenees: implications for reconstructing regional palaeoclimates. Palaeogeography,
999 Palaeoclimatology, Palaeoecology 305, 109–122.
1000 Delmas, M., Calvet, M., Gunnell, Y., Braucher, R., Bourlès, D., 2012. Les glaciations
1001 quaternaires dans les Pyrénées ariègeoises : approche historiographique, données
1002 paléogéographiques et chronologiques nouvelles. Quaternaire 23, 61–85.
1003 Delmas, M., Gunnell, Y., Calvet, M., Reixach, T., Oliva, M., 2021a. The Pyrenees: glacial
1004 landforms prior to the Last Glacial Maximum (Chapter 40). In Palacios, D., Hughes, P., García-
1005 Ruiz, J.M., Andrés, A., (eds), European glacial landscapes: maximum extent of glaciations.
1006 Elsevier, in press.
1007 Delmas, M., Gunnell, Y., Calvet, M., Reixach, T., Oliva, M., 2021b. The Pyrenees: glacial
1008 landforms from the Last Glacial Maximum (Chapter 59). In Palacios, D., Hughes, P., García-
1009 Ruiz, J.M., Andrés, A., (eds), European glacial landscapes: maximum extent of glaciations.
1010 Elsevier, in press.
1011 Dormoy, I., Peyron, O., Combourieu Nebout, N., Goring, S., Kotthoff, U., Magny, M., Pross, J.,
1012 2009. Terrestrial climate variability and seasonality changes in the Mediterranean region

between 15,000 and 4000 years BP deduced from marine pollen records. Climate of the Past 5, 615–632.

Dunne, J., Elmore, D., Muzikar, P., 1999. Scaling factors for the rates of production of cosmogenic nuclides for geometric shielding and attenuation at depth on sloped surfaces. Geomorphology 27, 3–11.

Eynaud, F., De Abreu, L., Voelker, A., Schönfeld, J., Salgueiro, E., Turon, J.L., Penaud, A., Toucanne, S., Naughton, F., Sánchez Goñi, M.F., Malaizé, B., Cacho, I., 2009. Position of the Polar Front along the western Iberian margin during key cold episodes of the last 45 ka. Geochemistry, Geophysics Geosystems 10, Q07U05, doi:10.1029/2009GC002398.

Fink, D., Vogt, S., Hotchkis, M., 2000. Cross-sections for ^{36}Cl from Ti at Ep = 35-150 MeV: applications to in-situ exposure dating. Nuclear Instrumentation Methods in Physics Research, Section B: Beam Interactions with Materials and Atoms 172, 861–866.

Fletcher, W.J, Sanchez Goñi, M.F., Peyron, O., Dormoy, I. 2010. Abrupt climate changes of the last deglaciation detected in a western Mediterranean forest record. Climate of the Past 6, 245–264.

Florineth, D., Schlüchter, C., 2000. Alpine evidence for atmospheric circulation patterns in Europe during the Last Glacial Maximum. Quaternary Research 54, 295–308.

García-Ruiz, J.M., Palacios, D., de Andrés, N., Valero-Garcés, B.L., López-Moreno, J.L., Sanjuán, Y., 2014. Holocene and 'Little Ice Age' glacial activity in the Marboré Cirque, Monte Perdido Massif, Central Spanish Pyrenees. The Holocene 24, 1–14.

García-Ruiz, J.M., Valero-Garcés, B.L., Martí-Bono, C., González-Sampériz, P., 2003. Asynchroneity of maximum glacier advances in the central Spanish Pyrenees. Journal of Quaternary Science 18, 61–72.

González-Sampériz, P., Aranbarri, J., Pérez-Sanz, A., Gil-Romera, G., Moreno, A., Leunda, M., Sevilla-Callejo, M., Corella, J.P., Morellón, M., Oliva, B., Valero-Garcés, B., 2017. Environmental and climate change in the southern Central Pyrenees since the Last Glacial Maximum: a view from the lake records. Catena 149, 668–688.

Gosse, J.C., Phillips, F.M., 2001. Terrestrial in situ cosmogenic nuclides: theory and application. Quaternary Science Reviews 20, 1475–1560.

Guerrero, J., Gutiérrez, F., García-Ruiz, J.M., Carbonel, D., Lucha, P., Arnold, L.J., 2018. Landslide-dam paleolakes in the Central Pyrenees, Upper Gállego River Valley, NE Spain: timing and relationship with deglaciation. Landslides 15, 1975–1989.

Haeberli, W., Penz, U., 1985. An attempt to reconstruct glaciological and climatological characteristics of 18 ka BP Ice Age glaciers in and around the Swiss Alps. Zeitschrift für Glazialkunde und Glazialgeologie 21, 351–361.

Harper, J. T., Humphrey, N.F., 2003. High altitude Himalayan climate inferred from glacial ice flux. Geophysical Research Letters 30, 1764–1767.

Hayes, A., Kučera, M., Kallel, N., Sbaffi, L., Rohling, E.J., 2005. Glacial Mediterranean sea surface temperatures based on planktonic foraminiferal assemblages. Quaternary Science Reviews 24, 999–1016.

Heyman, J., Stroeven, A.P., Harbor, J., Caffee, M.W., 2011. Too young or too old: evaluating cosmogenic exposure dating based on an analysis of compiled boulder exposure ages. Earth and Planetary Science Letters 302, 71–80.

Hock, R., 2003. Temperature index melt modelling in mountain areas. Journal of Hydrology 282, 104–115.

1058 Hofer, D., Raible, C.C., Dehnert, A., Kuhlemann, J., 2012. The impact of different glacial
1059 boundary conditions on atmospheric dynamics and precipitation in the North Atlantic
1060 region. Climate of the Past 8, 935–949.
1061 Hofmann, F.M., Alexanderson, H., Schoeneich, P., Mertes, J.R., Léanni, L., 2019. Post-Last
1062 Glacial Maximum glacier fluctuations in the southern Écrins massif (westernmost Alps):
1063 insights from ^{10}Be cosmic ray exposure dating. Boreas 48, 1019–1041.
1064 Hughes, A.L.C., Gyllencreutz, R., Lohne, Ø.S., Mangerud, J., Svendsen, J.I., 2016. The last
1065 Eurasian ice sheets - a chronological database and time-slice reconstruction, DATED-1.
1066 Boreas 45, 1–45.
1067 Hughes, P.D., Woodward, J.C., 2017. Quaternary glaciation in the Mediterranean mountains:
1068 A new synthesis. In: Hughes, P.D., Woodward, J.C. (eds), Quaternary glaciation in the
1069 Mediterranean mountains. Geological Society, London, Special Publication 433, 1–23.
1070 Ivy-Ochs, S., Kerschner, H., Kubik, P.W., Schluchter, C. 2006. Glacier response in the
1071 European Alps to Heinrich event 1 cooling: the Gschnitz stadial. Journal of Quaternary
1072 Science 21, 115–130.
1073 Ivy-Ochs, S., Kerschner, H., Reuther, A., Preusser, F., Heine, K., Maisch, M., Kubik, P.W.,
1074 Schlüchter, C., 2008. Chronology of the last glacial cycle in the European Alps. Journal of
1075 Quaternary Science 23, 559–573.
1076 Ivy-Ochs S. 2015. Glacier variations in the European Alps at the end of the last glaciation.
1077 Cuadernos de Investigación Geográfica 41, 295–315.
1078 Ivy-Ochs, S., Lucchesi, S., Baggio, P., Fioraso, G., Gianotti, F., Monegato, G., Graf, A.A., Akçar,
1079 N., Christl, M., Carraro, F., Forno, M.G., Schlüchter, C., 2018. New geomorphological and

chronological constraints for glacial deposits in the Rivoli-Avigliana end-moraine system and the lower Susa Valley (Western Alps, NW Italy). Journal of Quaternary Science 33, 550-562.

Jalut, G., Delibrias, G., Dagnac, J., Mardones, M., Bouhours, M., 1982. A palaeoecological approach to the last 21,000 years in the Pyrénées: the peat bog of Freychinède (alt. 1350 m, Ariège, South France). Palaeogeography, Palaeoclimatology, Palaeoecology 40, 321–359.

Jalut, G., Montserrat Marti, J., Fontugne, M., Delibrias, G., Vilaplana, J.M., Julia, R., 1992. Glacial to Interglacial vegetation changes in the northern and southern Pyrenees: deglaciation, vegetation cover and chronology. Quaternary Science Reviews 11, 449–480.

Jomelli, V., Chapron, E., Favier, V., Rinterknecht, V., Braucher, R., Tournier, N., Gascoin, S., Marti, R., Galop, D., Binet, S., Deschamps-Berger, C., Tissoux, H., Aumaître, G., Bourlès, D.L., Keddadouche, K., 2020. Glacier fluctuations during the Late Glacial and Holocene on the Ariège valley, northern slope of the Pyrenees and reconstructed climatic conditions. Mediterranean Geoscience Reviews 2, 37–51.

Jones, R.S., Small, D., Cahill, N., Bentley, M.J., Whitehouse, P.L., 2019. iceTEA: Tools for plotting and analysing cosmogenic-nuclide surface-exposure data from former ice margins. Quaternary Geochronology 51, 72–86.

Korschinek, G., Bergmaier, A., Faestermann, T., Gerstmann, U.C., Knie, K., Rugel, G., Wallner, A., Dillmann, I., Dollinger, G., von Gostomski, C.L., Kossert, K., Maiti, M., Poutivtsev, M., Remmert, A., 2010. A new value for the half-life of ^{10}Be by heavy ion elastic recoil detection and liquid scintillation counting. Nuclear Instrumentation Methods in Physics Research, Section B: Beam Interactions with Materials and Atoms 268, 187–191.

1101 Kuhlemann, J., Rohling, E.J., Krumrei, I., Kubik, P., Ivy-Ochs, S., Kucera, M., 2008. Regional
1102 synthesis of Mediterranean atmospheric circulation during the Last Glacial Maximum.
1103 Science 321, 1338–1340.
1104 Lal, D., 1991. Cosmic ray labeling of erosion surfaces: in situ nuclide production rates and
1105 erosion models. Earth and Planetary Science Letters 104, 424–439.
1106 Lambeck, K., Rouby, H., Purcell, A., Sun, Y., Sambridge, M., 2014. Sea level and ice volume
1107 since the glacial maximum. Proceedings of the National Academy of Sciences 111, 15296–
1108 15303.
1109 Laskar, J., Robutel, P., Joutel, F., Gastineau, M., Correia, A.C.M., Levrard, B., 2004. A long-
1110 term numerical solution for the insolation quantities of the Earth. Astronomy and
1111 Astrophysics 428, 261–285.
1112 Lewis, C.J., Mc Donald, E.V., Sancho, C., Peña, J.L., Rhodes, E.J., 2009. Climatic implications of
1113 correlated Upper Pleistocene and fluvial deposits on the Cinca and Gállego Rivers (NE Spain)
1114 based on OSL dating and soil stratigraphy. Global and Planetary Change 67, 141–152.
1115 Lisiecki, L.E., Raymo, M.E., 2005. A Pliocene-Pleistocene stack of 57 globally distributed
1116 benthic δ18O records. Paleoceanography 20, PA1003.
1117 López-Moreno, J.I., 2006. Cambio ambiental y gestión de embalses en el Pirineo Central
1118 Español. Consejo de Protección de la Naturaleza de Aragón. Zaragoza, 260 p.
1119 Ludwig, P., Schaffernicht, E.J., Shao, Y., Pinto, J.G., 2016. Regional atmospheric circulation
1120 over Europe during the Last Glacial Maximum and its links to precipitation. Journal of
1121 Geophysical Research: Atmospheres 121, 2130–2145.

1122 Luetscher, M., Boch, R., Sodemann, H., Spötl, C., Cheng, H., Edwards, R.L., Frisia, S., Hof, F.,
1123 Müller, W., 2015. North Atlantic storm track changes during the Last Glacial Maximum
1124 recorded by Alpine speleothems. Nature Communications 6, 6344.
1125 Maffezzoli, N., Vallelonga, P., Edwards, R., Saiz-Lopez, A., Turetta, C., Astrid Kjær, H.,
1126 Barbante, C., Vinther, B., Spolaor, A., 2019. A 120,000-year record of sea ice in the North
1127 Atlantic? Climate of the Past 15, 2031–2051.
1128 Makos, M., Nitychoruk, J., Zreda, M., 2012. The Younger Dryas climatic conditions, Polish
1129 High Tatra Mountains. Boreas 42, 745–761.
1130 Makos, M., Rinterknecht, V., Braucher, R., Toloczko-Pasek, A., Aster Team, 2018. Last Glacial
1131 Maximum and Lateglacial in the Polish High Tatra Mountains — Revised deglaciation based
1132 on the ^{10}Be exposure age dating. Quaternary Science Reviews 187, 130–156.
1133 Marti, R., 2016. Apport des méthodes de télédétection à très haute résolution spatiale dans
1134 l'étude des variations de la cryosphère des Pyrénées. Unpubl. PhD thesis, Université
1135 Toulouse le Mirail-Toulouse II, 273 p.
1136 Martin, L.C.P., Blard, P.-H., Balco, G., Lavé, J., Delunel, R., Lifton, N., Laurent, V., 2017. The
1137 CREp program and the ICE-D production rate calibration database: a fully parameterizable
1138 and updated online tool to compute cosmic-ray exposure ages. Quaternary Geochronology
1139 38, 25–49.
1140 Melki, T., Kallel, N., Jorissen, F.J., Guichard, F., Dennielou, B., Berné, S., Labeyrie, L.,
1141 Fontugne, M., 2009. Abrupt climate change, sea surface salinity and paleoproductivity in the
1142 western Mediterranean Sea (Gulf of Lion) during the last 28 kyr. Palaeogeography,
1143 Palaeoclimatology, Palaeoecology 279, 1–2, 96–113.

1144 Merchel, S., Arnold, M., Aumaître, G., Benedetti, L., Bourlès, D.L., Braucher, R., Alfimov, V.,
1145 Freeman, S.P.H.T., Steier, P., Wallner, A., 2008. Towards more precise ^{10}Be and ^{36}Cl data
1146 from measurements at the 10−14 level: influence of sample preparation. Nuclear
1147 Instrumentation Methods in Physics Research, Section B: Beam Interactions with Materials
1148 and Atoms 266, 4921–4926.
1149 Merz, N., Raible, C.C., Woollings, T., 2015. North Atlantic eddy-driven jet in interglacial and
1150 glacial winter climates. Journal of Climate 28, 3977–3997.
1151 Millet, L., Rius, D., Galop, D., Heiri, O., Brooks, S.J., 2012. Chironomid-based reconstruction of
1152 Late-Glacial summer temperatures from the Ech palaeolake record (French western
1153 Pyrenees). Palaeogeography, Palaeoclimatology, Palaeoecology 315, 86–99.
1154 Mix, A.C., Bard, E., Schneider, R., 2001. Environmental processes of the ice age: land, oceans,
1155 glaciers (EPILOG). Quaternary Science Reviews 20, 627–657.
1156 Monegato, G., Scardia, G., Hajdas, I., Rizzini, F., Piccin, A., 2017. The Alpine LGM in the boreal
1157 icesheets game. Scientific Reports 7, 2078.
1158 Monegato, G., Ravazzi, C., 2018. The Late Pleistocene Multifold glaciation in the Alps:
1159 updates and open questions. Alpine and Mediterranean Quaternary 31, 225-229.
1160 Moreno, A., González-Sampériz, P., Morellón, M., Valero-Garcés, B.L., Fletcher, W.J., 2012.
1161 Northern Iberian abrupt climate change dynamics during the last glacial cycle: a view from
1162 lacustrine sediments. Quaternary Science Reviews 36, 139–153.
1163 Moreno, A., Svensson, A., Brooks, S.J., Connor, S., Engels, S., Fletcher, W., Genty, D., Heiri, O.,
1164 Labuhn, I., Persoiu, A., Peyron, O., Sadori, L., Valero-Garces, B., Wulf, S., Zanchetta G., 2014.
1165 A compilation of Western European terrestrial records 60e8 ka BP: towards an
1166 understanding of latitudinal climatic gradients. Quaternary Science Reviews 106, 167–185.

1167 Muscheler, R., Beer, J., W. Kubik, P., H-A, Synal., 2005. H-A Geomagnetic field intensity
1168 during the last 60,000 years based on ^{10}Be and ^{36}Cl from the Summit ice cores and ^{14}C.
1169 Quaternary Science Reviews 24, 16–17.
1170 Naughton, F., Costas, S., Gomes, S.D., Desprat, S., Rodrigues, T., Sanchez Goñi, M.F.,
1171 Renssen, H., Trigo, R., Bronk-Ramsey, C., Oliveira, D., Salgueiro, E., Voelker, A.H.L., Abrantes,
1172 F., 2019. Coupled ocean and atmospheric changes during Greenland stadial 1 in
1173 southwestern Europe. Quaternary Science Reviews 212, 108–120.
1174 Nishiizumi, K., Winterer, E.L., Kohl, C.P., Klein, J., Middleton, R., Lal, D., Arnold, J.R., 1989.
1175 Cosmic ray production rates of ^{10}Be and ^{26}Al in quartz from glacially polished rocks. Jounal of
1176 Geophyical Research: Solid Earth 94, 17907–17915.
1177 Nishiizumi, K., Imamura, M., Caffee, M., Southon, J., Finkel, R., 2007. Absolute calibration of
1178 ^{10}Be AMS standards. Nuclear Instruments and Methods in Physics Research Section B: Beam
1179 Interactions with Materials and Atoms 258, 403–413.
1180 Oliva-Urcia, B., Moreno, A., Leunda, M., Valero-Garcés, B., González-Sampériz, P., Gil-
1181 Romera, G., Mata, M.P., HORDA Group, 2017. Last deglaciation and Holocene environmental
1182 change at high altitude in the Pyrenees: the geochemical and paleomagnetic record from
1183 Marboré Lake (N Spain). Journal of Paleolimnology 59, 349–371.
1184 Palacios, D., de Andrés, N., López-Moreno, J.I., García-Ruiz, J.M. 2015a. Late Pleistocene
1185 deglaciation in the central Pyrenees: the upper Gállego valley. Quaternary Research 83, 397–
1186 414.
1187 Palacios, D., Gómez-Ortiz, A., de Andrés, N., Vázquez-Selem, L., Salvador-Franch, F., Oliva, M.
1188 2015b. Maximum Extent of Late Pleistocene Glaciers and Last Deglaciation of La Cerdanya
1189 Mountains, Southeastern Pyrenees. Geomorphology 231, 116–129.

1190 Palacios, D., García-Ruiz, J.M., Andrés, N., Schimmelpfennig, I., Campos, N., Léanni, L., ASTER
1191 Team, 2017. Deglaciation in the central Pyrenees during the Pleistocene-Holocene transition:
1192 timing and geomorphological significance. Quaternary Science Reviews 162, 111–127.
1193 Paillard, D., Labeyrie, L., Yiou, P., 1996. Macintosh Program performs time-series analysis.
1194 Eos, Transactions American Geophysical Union 77, 379–379.
1195 Pallàs, R., Rodés, A., Braucher, R., Carcaillet, J., Ortuño, M., Bordonau, J., Bourlès, D.,
1196 Vilaplana, J.M., Masana, E., Santanach, P., 2006. Late Pleistocene and Holocene glaciation in
1197 the Pyrenees: a critical review and new evidence from ^{10}Be exposure ages, south-central
1198 Pyrenees. Quaternary Science Reviews 25, 2937–1963.
1199 Pallàs, R., Rodés, A., Braucher, R., Bourlès, D., Delmas, M., Calvet, M., Gunnell, Y., 2010.
1200 Small, isolated glacial catchments as priority targets for cosmogenic surface exposure dating
1201 of Pleistocene climate fluctuations, southeastern Pyrenees. Geology 38, 891–894.
1202 Pellitero, R., Rea, B.R., Spagnolo, M., Bakke, J., Ivy-Ochs, S., Frew, C.R., Hughes, P., Ribolini,
1203 A., Lukas, S., Renssen, H., 2016. Glare, a GIS tool to reconstruct the 3D surface of
1204 palaeoglaciers. Computers & Geosciences 94, 77–85.
1205 Pellitero, R., Fernández-Fernández, J.M., Campos, N., Serrano, E., Pisabarro, A., 2019. Late
1206 Pleistocene climate of the northern Iberian Peninsula: New insights from palaeoglaciers at
1207 Fuentes Carrionas (Cantabrian Mountains). Journal of Quaternary Science 34, 342–354.
1208 Phillips, F.M., Stone, W.D., Fabryka-Martin, J.T., 2001. An improved approach to calculating
1209 low-energy cosmic-ray neutron fluxes near the land/atmosphere interface. Chemical
1210 Geology 175, 689–701.
1211 Protin, M., Schimmelpfennig, I., Mugnier, J.-L., Ravanel, L., Le Roy, M., Deline, P., Favier, V.,
1212 Buoncristiani, J.F., Aster Team. 2019. Climate reconstruction for the Younger Dryas/early

1213 Holocene transition and the Little Ice Age based on paleo extents of Argentiere glacier
1214 (French Alps). Quaternary Science Reviews 221, 105883.
1215 Prud'homme, C., Vassallo, R., Crouzet, C., Carcaillet, J., Mugnier, J.-L., Cortés-Aranda, J.,
1216 2020. Paired ^{10}Be sampling of polished bedrock and erratic boulders to improve dating of
1217 glacial landforms: an example from the Western Alps. Earth Surface Processes and
1218 Landforms 45, 1168–1180.
1219 Rasmussen, S.O., Bigler, M., Blockley, S.P., Blunier, T., Buchardt, S.L., Clausen, H.B.,
1220 Cvijanovic, I., Dahl-Jensen, D., Johnsen, S.J., Fischer, H., Gkinis, V., Guillevic, M., Hoek, W.Z.,
1221 Lowe, J.J., Pedro, J.B., Popp, T., Seierstad, I.K., Steffensen, J.P., Svensson, A.M., Vallelonga, P.,
1222 Vinther, B.M., Walker, M.J.C., Wheatley, J.J., Winstrup, M., 2014. A stratigraphic framework
1223 for abrupt climatic changes during the Last Glacial period based on three synchronized
1224 Greenland ice-core records: refining and extending the INTIMATE event stratigraphy.
1225 Quaternary Science Reviews 106, 14–28.
1226 Reille, M., Andrieu, V., 1993. Variations de la limite supérieure des forêts dans les Pyrénées
1227 (France) pendant le Tardiglaciaire. Compte rendu de l'Académie des Sciences de Paris Série II
1228 316, 547–551.
1229 Reille, M., Lowe, J.J., 1993. A re-evaluation of the vegetation history of the eastern Pyrenees
1230 (France) from the end of the Last Glacial to the Present. Quaternary Science Reviews 12, 47–
1231 77.
1232 Rea, B.R., 2009. Defining modern day area-altitude balance ratios (AABRs) and their use in
1233 glacier-climate reconstructions. Quaternary Science Reviews 28, 237-248.

1234 Rea, B.R., Pellitero, R., Spagnolo, M., Hughes, P., Ivy-Ochs, S., Renssen, H., Ribolini, A., Bakke,
1235 J., Lukas, S., Braithwaite, R.J., 2020. Atmospheric circulation over Europe during the Younger
1236 Dryas. Science Advances 6, 1–14.
1237 Rius, D., Galop, D., Doyen, E., Millet, L., Vannière, B., 2014. Biomass burning response to
1238 high-amplitude climate and vegetation changes in Southwestern France from the Last Glacial
1239 to the early Holocene. Vegetation History and Archaeobotany 23, 729–742.
1240 Rodrigo-Gámiz, M., Martínez-Ruiz, F., Jiménez-Espejo, F.J., Gallego-Torres, D., Nieto-Moreno,
1241 V., Romero, O., Ariztegui, D., 2011. Impact of climate variability in the western
1242 Mediterranean during the last 20,000 years: oceanic and atmospheric responses. Quaternary
1243 Science Reviews 30, 2018–2034.
1244 Sarikaya, M.A., Zreda, M., Ciner, A., 2009. Glaciations and paleoclimate of Mount Erciyes,
1245 central Turkey, since the Last Glacial Maximum, inferred from ^{36}Cl cosmogenic dating and
1246 glacier modeling. Quaternary Science Reviews 28, 2326–2341.
1247 Schimmelpfennig, I., 2009. Cosmogenic Cl-36 in Ca and K Rich Minerals: Analytical
1248 Developments, Production Rate Calibrations and Cross Calibration with He-3 and Ne-21. PhD
1249 Thesis, Université Paul Cezanne Aix–Marseille III, CEREGE, Aix en Provence, France, 343 p.
1250 Schimmelpfennig, I., Benedetti, L., Finkel, R., Pik, R., Blard, P.-H., Bourles, D., Burnard, P.,
1251 Williams, A., 2009. Sources of in-situ ^{36}Cl in basaltic rocks. Implications for calibration of
1252 production rates. Quaternary Geochronology 4, 441–461.
1253 Seguinot, J., Jouvet, G., Huss, M., Funk, M., Ivy-Ochs, S., Preusser, F., 2018. Modelling last
1254 glacial cycle dynamics in the Alps. The Cryosphere 12, 3265–3285.
1255 Six, D., Vincent, C., 2014. Sensitivity of mass balance and equilibrium line altitude to climate
1256 change in the French Alps. Journal of Glaciology 60, 874–878.

1257 Stone, J.O., 2000. Air pressure and cosmogenic isotope production. Journal of Geophysical
1258 Research 105 (B10), 23753–23759.
1259 Stone, J.O., Fifield, K., Vasconcelos, P., 2005. Terrestrial chlorine-36 production from
1260 spallation of iron. In: Abstract of 10th International Conference on Accelerator Mass
1261 Spectrometry. September 5–10, 2005, Berkeley, USA.
1262 Stokes, C.R., Tarasov, L., Dyke, A.S., 2012. Dynamics of the North American Ice Sheet
1263 Complex during its inception and build-up to the Last Glacial Maximum. Quaternary Science
1264 Reviews 50, 86–104.
1265 Tomkins, M., Huck, J., Dortch, J., Hughes, P., Kirkbride, M., Barr, I., 2018. Schmidt Hammer
1266 exposure dating (SHED): Calibration procedures, new exposure age data and an online
1267 calculator. Quaternary Geochronology 44, 55–62.
1268 Thompson, W.G., Goldstein, S.L., 2006. A radiometric calibration of the SPECMAP timescale.
1269 Quaternary Science Reviews 25, 3207–3215.
1270 Uppala, S.M., KÅllberg, P.W., Simmons, A.J., Andrae, U., Bechtold, V.D.C., Fiorino, M.,
1271 Gibson, J.K., Haseler, J., Hernandez, A., Kelly, G.A., Li, X., Onogi, K., Saarinen, S., Sokka, N.,
1272 Allan, R.P., Andersson, E., Arpe, K., Balmaseda, M.A., Beljaars, A.C.M., Berg, L.V.D., Bidlot, J.,
1273 Bormann, N., Caires, S., Chevallier, F., Dethof, A., Dragosavac, M., Fisher, M., Fuentes, M.,
1274 Hagemann, S., Hólm, E., Hoskins, B.J., Isaksen, L., Janssen, P.A.E.M., Jenne, R., McNally, A.P.,
1275 Mahfouf, J.-F., Morcrette, J.-J., Rayner, N.A., Saunders, R.W., Simon, P., Sterl, A., Trenberth,
1276 K.E., Untch, A., Vasiljevic, D., Viterbo, P., Woollen, J., 2005. The ERA-40 re-analysis. Quarterly
1277 Journal of the Royal Meteorological Society 131, 2961–3012.
1278 Vermeesch, P., 2007. CosmoCalc: an Excel add-in for cosmogenic nuclide calculations
1279 Geochemistry, Geophysics, Geosystems 8, Q08003, doi:10.1029/2006GC001530.

Figure 1. The Late Pleistocene Pyrenean icefield (after Calvet et al., 2011; Delmas et al., 2011). 1- Local LGM (LLGM, MIS 4 or MIS 3). 2- Pyrenean ice extent at the time of the LGM (29–19 ka). a- LGM glacier fronts very close (typically <0.5 km) to the LLGM position. b- LGM glacier fronts located ~10 km upstream from the LLGM position. c- LGM glacier fronts believed to be located more than 20 km upstream from the LLGM but not yet mapped with great accuracy. 3- Published studies on Last Glacial-to-Interglacial Termination (LGIT) and Holocene ice fluctuations. a- Data based on TCN exposure ages. b- Data based on radiocarbon ages.

Figure 2. Modern climatic conditions and Late Pleistocene glaciation in the eastern Pyrenees. Map frames in A, B and C are identical. A, B: present-day mean annual surface air temperature and total annual precipitation values (generated from data in Batalla et al., 2018). Red dashes: Atlantic/Mediterranean drainage divide, which was also the Late Pleistocene ice divide. C: Late Pleistocene ice limits and location of research focus areas. Black and blue rectangles: areas mapped in Figure 5, and in Figures 9 and 11, respectively. White squares locate the lacustrine sequences cited in the text: 1- Ruisseau de Laurenti; 2- Balcère; 3- La Borde; 4- Freychinède; 5- La Moulinasse. Weather stations used for paleoclimate modeling (numbered red circles): 1- Foix; 2- Tarascon; 3- Vicdessos; 4- Montferrier; 5- Verdun; 6- Ascou; 7- Hospitalet; 8- Malniu; 9- Das; 10- La Molinas; 11- Puigcerdà; 12- Targasonne; 13- Saillagouse; 14- Mont Louis; 15- Col de la Quillane; 16- Formiguères.

Figure 3. Examples of boulders sampled for ^{10}Be surface exposure dating in the upper Ariège catchment.

Figure 4. Method for paleoclimate reconstructions: example based on the Petches/Ax-les-Thermes stadial position. A- Ice-thickness reconstruction using the Glare ArcGis™ toolbox. Light blue line: ice thickness variation along the flowline. The dark and bold blue sections locate the lateral moraines used to constrain the longitudinal glacier profile, ice thickness, and 3-D ice surface of the glacial stillstand. Black line: topography of the glacier bed inferred from the 5 m DEM along the ice flowline, manually drawn on the basis on the present-day slope morphology; ac: accumulation area; ab: ablation area; CS1, CS2, CS3: cross-sections used for calculating the F value in equations (1) and (2). B- Current surface mass-balance curve modeled following Harper and Humphrey (2003). C- Paleoclimatic conditions (summarized as precipitation–temperature pairs) relative to present values obtained from the glaciological models and the Harper and Humphrey (2003) application. Light blue line links all the P and T pairs suited to generating the Petches/Ax stadial ice extent under constraints of a *DDF* value of 3.0 mm eq. water·°C^{-1}·day^{-1} for snow and of 6.1 mm eq. water·°C^{-1}·day^{-1} for ice. Light blue shading covers all P and T pairs suited to generating the Petches/Ax stadial ice extent when accounting for *DDF* variability as recorded worldwide among temperate glaciers. Blue circles show P and T pairs, each corresponding to a given ice thickness, ELA, and mass balance gradient (MBG).

Figure 5. Geomorphological maps of Pleistocene landforms and deposits and ^{10}Be surface exposure ages obtained in the downstream part (A) and upstream part (B) of the upper

Ariège catchment. Ages indicated in gray are not used in the modeling for reasons explained in Section 4.1.2. Brown stars in B: gneiss boulders. Elevation contour interval: 100 m.

Figure 6. 3-D glacier configurations during each of the four glacial stillstands (local stades) identified in the upper Ariège catchment.

Figure 7. ^{10}Be exposure ages and their probability density plots for the upper Ariège catchment. Samples are arranged by sampling site and associated by stadial ice extent. White circles: samples considered as outliers for reasons explained in Section 4.1.2.

Figure 8. Reconstructed P and T pairs relative to present conditions, here applied to the four glacial stillstands (local stades) identified in the upper Ariège catchment.

Figure 9. 3-D glacier configurations during each of the glacial stillstands identified in the northern massifs of the eastern Pyrenees. Panel G: probability density plots of ^{10}Be exposure ages.

Figure 10. Reconstructed P and T pairs relative to present conditions, here applied to the glacial stillstands identified in the Vicdessos catchment.

Figure 11. 3-D glacier configurations applied to the glacial stillstands identified among the southern massifs of the eastern Pyrenees. A to C: method as in Figures 7 and 9. D: method and abbreviations as in Figure 4. Panel E: Probability density plots of ^{10}B ages.

Figure 12. East-Pyrenean paleoclimate within a multi-proxy European setting. Note that data for the southern massifs are lacking from GI-1 onward because glaciers by that time had become very small or extinct. Data sources as follows: Cantabrian Mountains: Pellitero et al. (2019); High Tatra: Makos et al. (2012, 2018); European Alps: Ivy-Ochs et al. (2006, 2008), Protin et al. (2019); central Pyrenees (Ech chironomid assemblage): Millet et al. (2012), and speleothem geochemistry of Seso Cave: Bartolomé et al. (2015); NW Iberia (Laguna de la Roya chironomid assemblage): Muñoz Sobrino et al. (2012); Alborán Sea (pollen-inferred climate reconstruction, annual T and P anomalies): Combourieu-Nebout et al. (2009), Rodrigo-Gámiz et al. (2011). Levantine Sea (TEX86-based SST estimates): Castañeda et al. (2010); Alborán Sea (UK37-index-based SST estimates): Cacho et al., 1999; Tyrrhenian Sea (UK37-index-based SST estimates): Cacho et al., 2001; Gulf of Lion SST (April–May) derive from planktonic foraminiferal assemblages: Melki et al. (2009). June insolation at 40°N: after Laskar et al. (2004), calculated using AnalySeries 2.0 (Paillard et al., 1996). Evolution of sea-ice extent (based on bromine enrichment): Maffezzoli et al. (2019). Ice volume evolution of the Fennoscandian Ice Sheet: Hughes et al. (2015). Ice volume evolution of the North American Ice Sheet: Stokes et al. (2012). Pleistocene sea-level reconstructions: Lambeck et al. (2014); GRIP and NGRIP stratigraphies: Rasmussen et al. (2014).

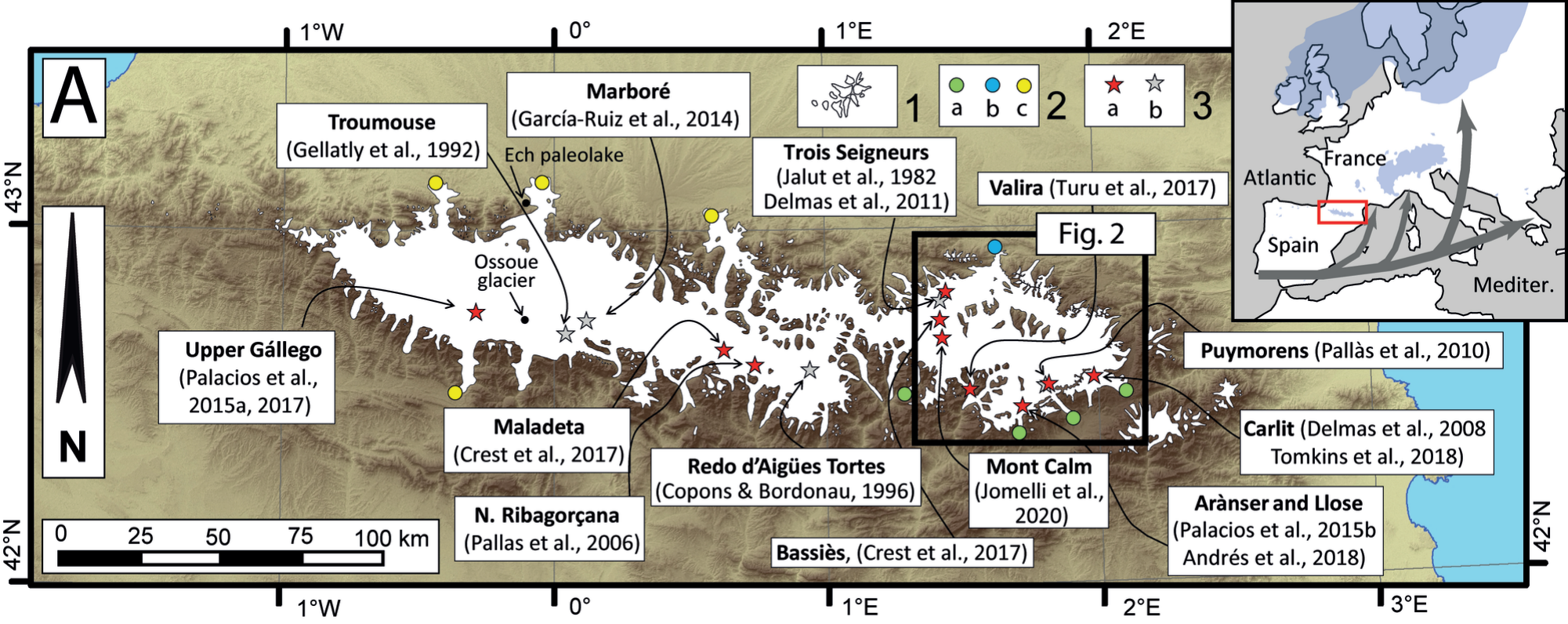
A
1°W
0°
1°E
2°E
3°E
43°N
42°N
N
0 25 50 75 100 km
1
2
a b c
3
a b
Troumouse
(Gellatly et al., 1992)
Marboré
(García-Ruiz et al., 2014)
Ech paleolake
Trois Seigneurs
(Jalut et al., 1982
Delmas et al., 2011)
Valira (Turu et al., 2017)
Fig. 2
Ossoue
glacier
Upper Gállego
(Palacios et al.,
2015a, 2017)
Maladeta
(Crest et al., 2017)
Redo d'Aigües Tortes
(Copons & Bordonau, 1996)
N. Ribagorçana
(Pallas et al., 2006)
Bassiès, (Crest et al., 2017)
Mont Calm
(Jomelli et al.,
2020)
Puymorens (Pallàs et al., 2010)
Carlit (Delmas et al., 2008
Tomkins et al., 2018)
Aránser and Llose
(Palacios et al., 2015b
Andrés et al., 2018)
Atlantic
France
Spain
Mediter.

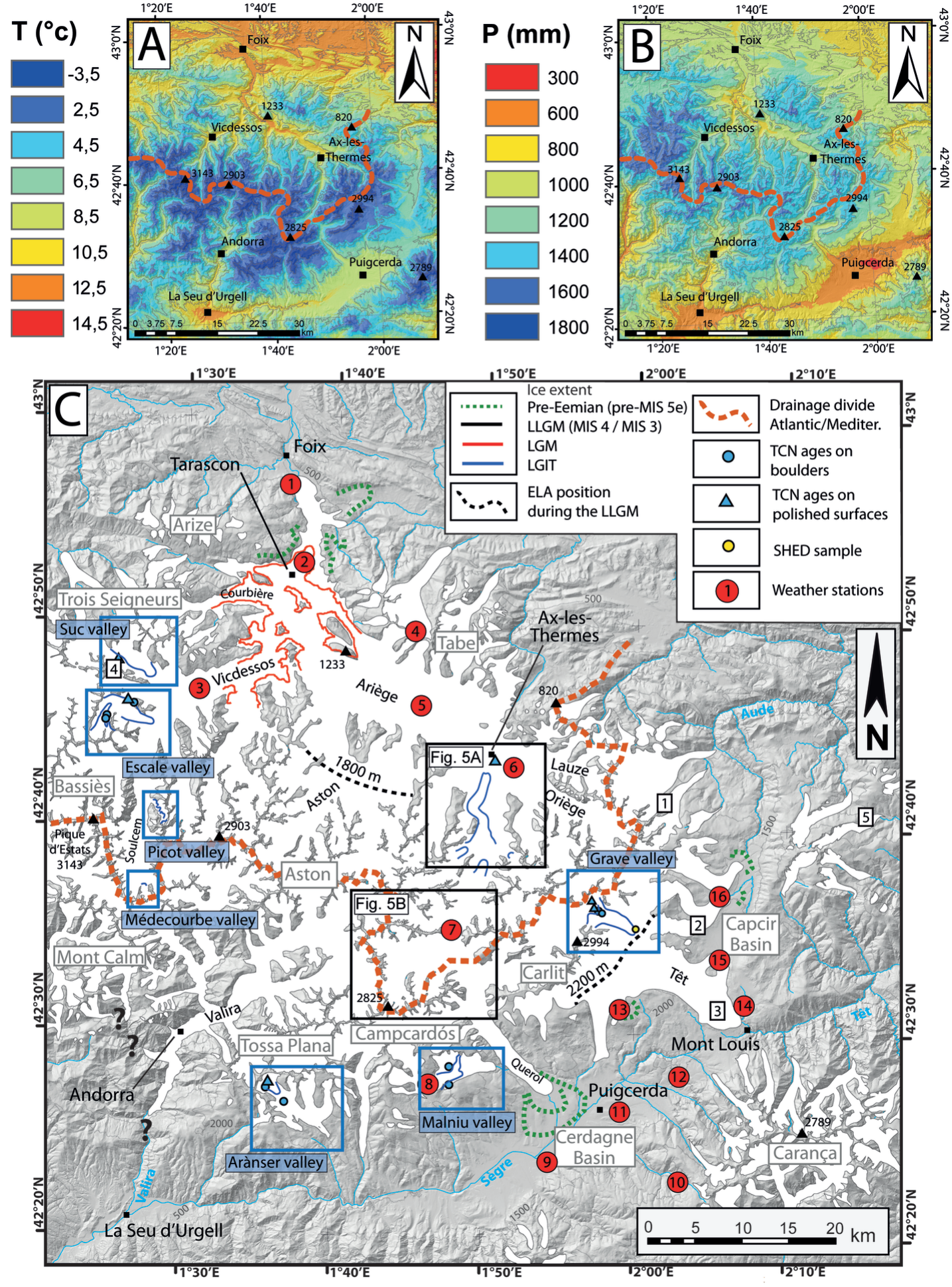
T (°c)
-3,5
2,5
4,5
6,5
8,5
10,5
12,5
14,5
A
B
P (mm)
300
600
800
1000
1200
1400
1600
1800
N
Foix
Vicdessos
Ax-les-Thermes
Andorra
Puigcerda
La Seu d'Urgell
1233
820
3143
2903
2994
2825
2789
0 3.75 7.5 15 22.5 30 km
1°20'E
1°40'E
2°00'E
43°0'N
42°40'N
42°20'N
C
1°30'E
1°40'E
1°50'E
2°00'E
2°10'E
43°N
42°50'N
42°40'N
42°30'N
42°20'N
Ice extent
Pre-Eemian (pre-MIS 5e)
LLGM (MIS 4 / MIS 3)
LGM
LGIT
ELA position during the LLGM
Drainage divide Atlantic/Mediter.
TCN ages on boulders
TCN ages on polished surfaces
SHED sample
Weather stations
Tarascon
Arize
Trois Seigneurs
Suc valley
Escale valley
Bassiès
Pique d'Estats 3143
Soulcem
Picot valley
Médecourbe valley
Mont Calm
Courbière
Tabe
Ariège
Vicdessos
Ax-les-Thermes
Aston
1800 m
Fig. 5A
Fig. 5B
Lauze
Oriège
Aude
Grave valley
Capcir Basin
Carlit
2200 m
Têt
Mont Louis
Campcardós
Tossa Plana
Valira
Andorra
Aránser valley
Malniu valley
Querol
Puigcerda
Cerdagne Basin
Carança
Ségre
La Seu d'Urgell
0 5 10 15 20 km

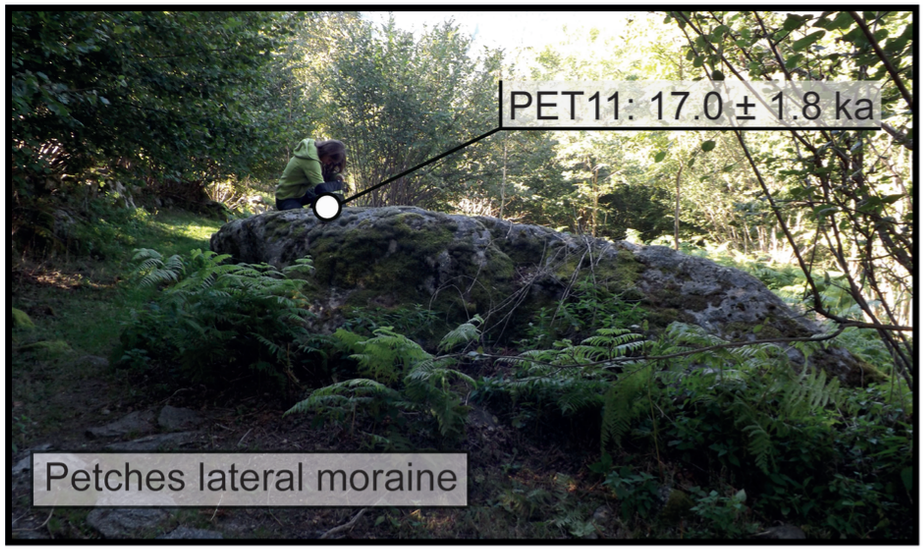
PET11: 17.0 ± 1.8 ka
Petches lateral moraine

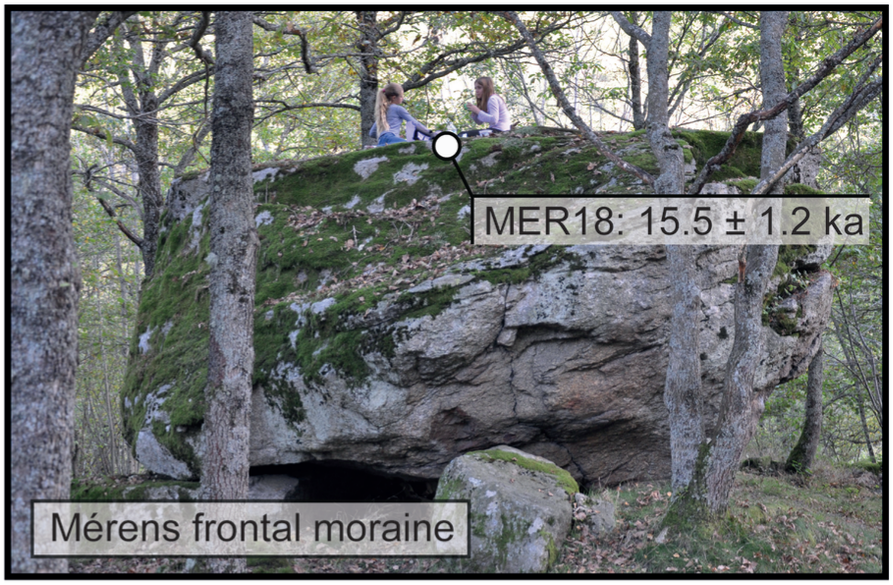
MER18: 15.5 ± 1.2 ka
Mérens frontal moraine

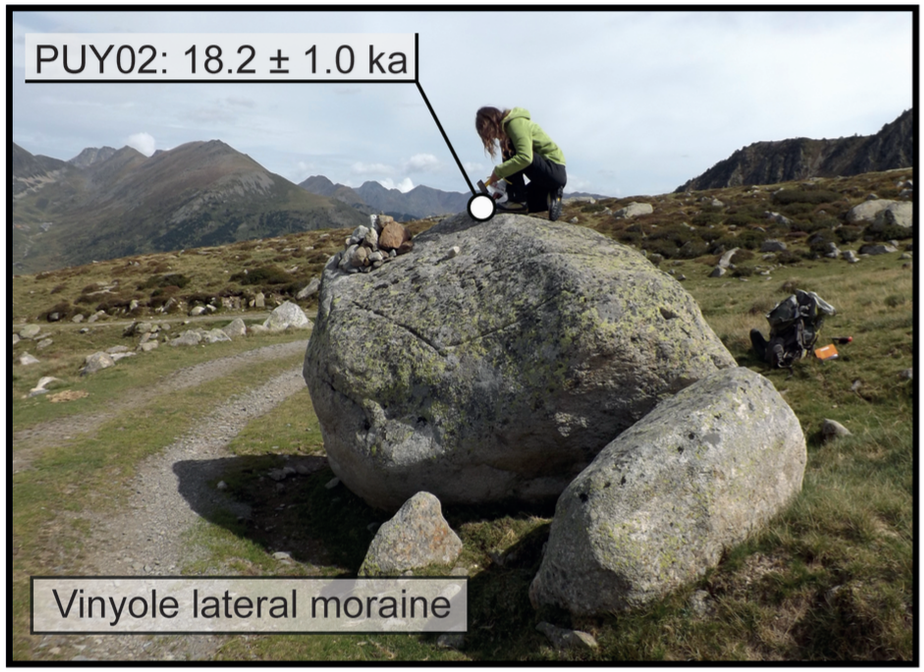
PUY02: 18.2 ± 1.0 ka
Vinyole lateral moraine

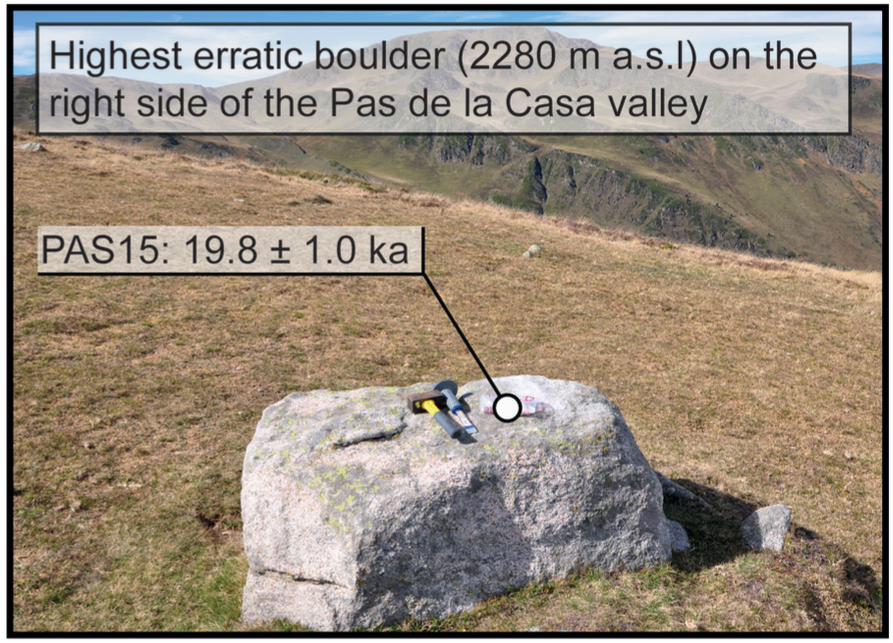
Highest erratic boulder (2280 m a.s.l) on the right side of the Pas de la Casa valley
PAS15: 19.8 ± 1.0 ka

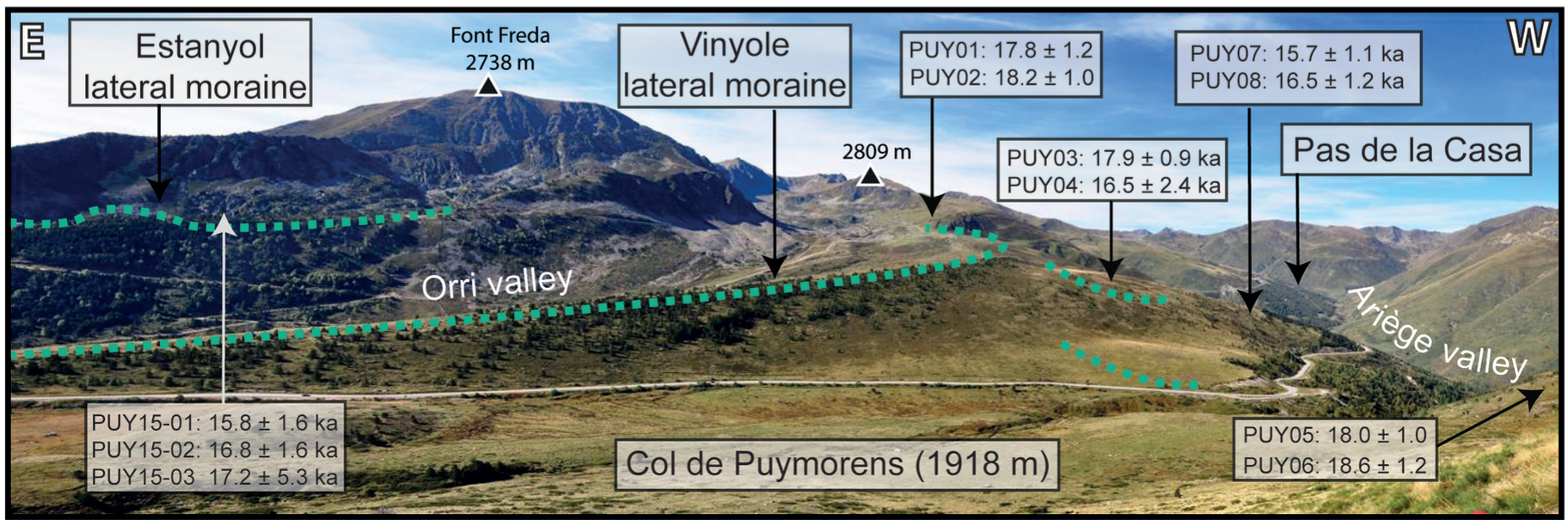
E
W
Estanyol lateral moraine
Font Freda 2738 m
Vinyole lateral moraine
PUY01: 17.8 ± 1.2
PUY02: 18.2 ± 1.0
PUY07: 15.7 ± 1.1 ka
PUY08: 16.5 ± 1.2 ka
2809 m
PUY03: 17.9 ± 0.9 ka
PUY04: 16.5 ± 2.4 ka
Pas de la Casa
Orri valley
Ariège valley
PUY15-01: 15.8 ± 1.6 ka
PUY15-02: 16.8 ± 1.6 ka
PUY15-03 17.2 ± 5.3 ka
Col de Puymorens (1918 m)
PUY05: 18.0 ± 1.0
PUY06: 18.6 ± 1.2

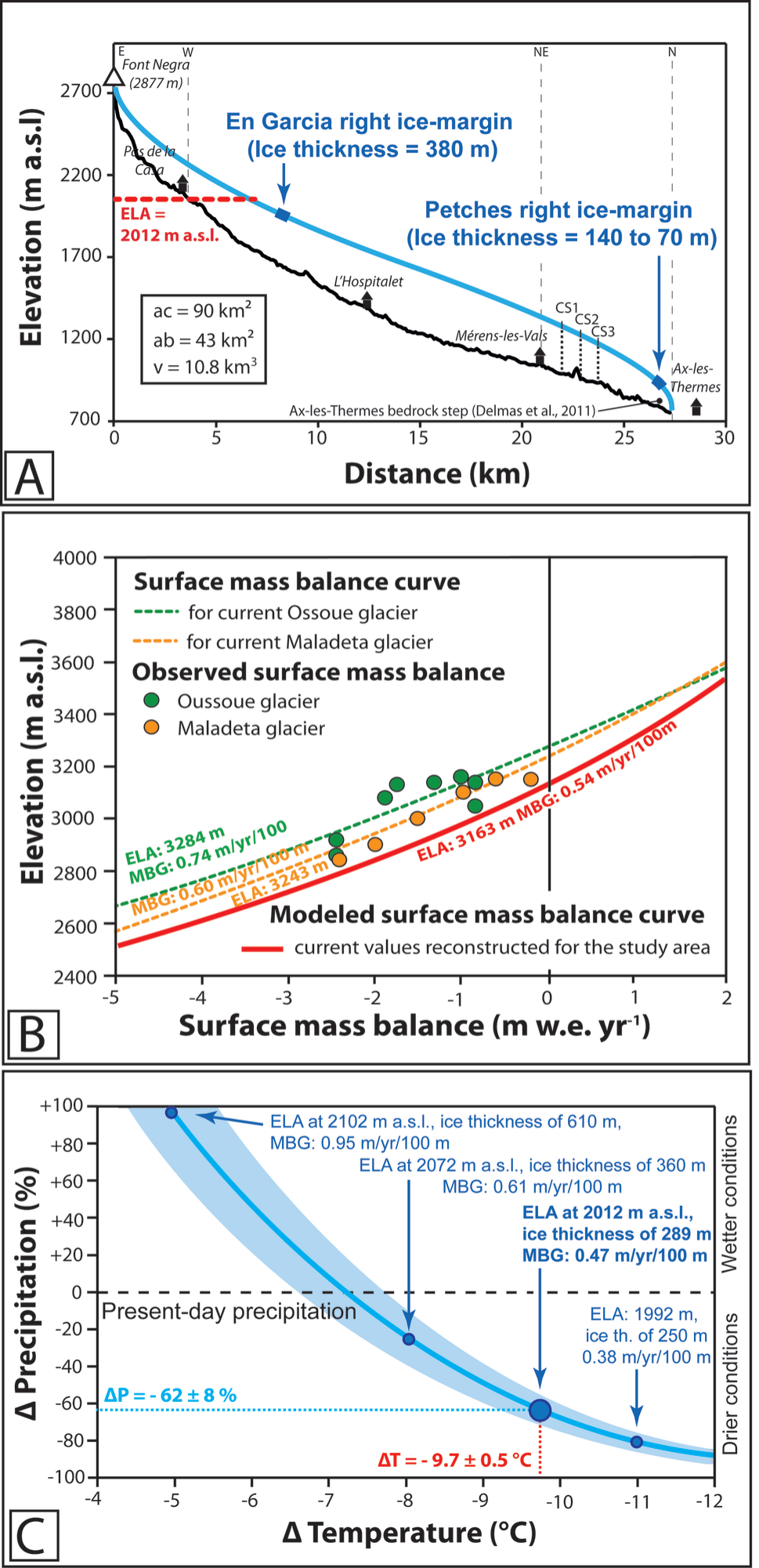
A
E
W
NE
N
Font Negra
(2877 m)
Pas de la Casa
En Garcia right ice-margin
(Ice thickness = 380 m)
Petches right ice-margin
(Ice thickness = 140 to 70 m)
ELA =
2012 m a.s.l.
L'Hospitalet
CS1
CS2
CS3
Mérens-les-Vals
Ax-les-Thermes
ac = 90 km²
ab = 43 km²
v = 10.8 km³
Ax-les-Thermes bedrock step (Delmas et al., 2011)
Elevation (m a.s.l)
Distance (km)
B
Surface mass balance curve
for current Ossoue glacier
for current Maladeta glacier
Observed surface mass balance
Oussoue glacier
Maladeta glacier
ELA: 3284 m
MBG: 0.74 m/yr/100
MBG: 0.60 m/yr/100 m
ELA: 3243 m
ELA: 3163 m MBG: 0.54 m/yr/100m
Modeled surface mass balance curve
current values reconstructed for the study area
Elevation (m a.s.l.)
Surface mass balance (m w.e. yr⁻¹)
C
ELA at 2102 m a.s.l., ice thickness of 610 m,
MBG: 0.95 m/yr/100 m
ELA at 2072 m a.s.l., ice thickness of 360 m
MBG: 0.61 m/yr/100 m
ELA at 2012 m a.s.l.,
ice thickness of 289 m
MBG: 0.47 m/yr/100 m
Present-day precipitation
ELA: 1992 m,
ice th. of 250 m
0.38 m/yr/100 m
ΔP = - 62 ± 8 %
ΔT = - 9.7 ± 0.5 °C
Wetter conditions
Drier conditions
Δ Precipitation (%)
Δ Temperature (°C)

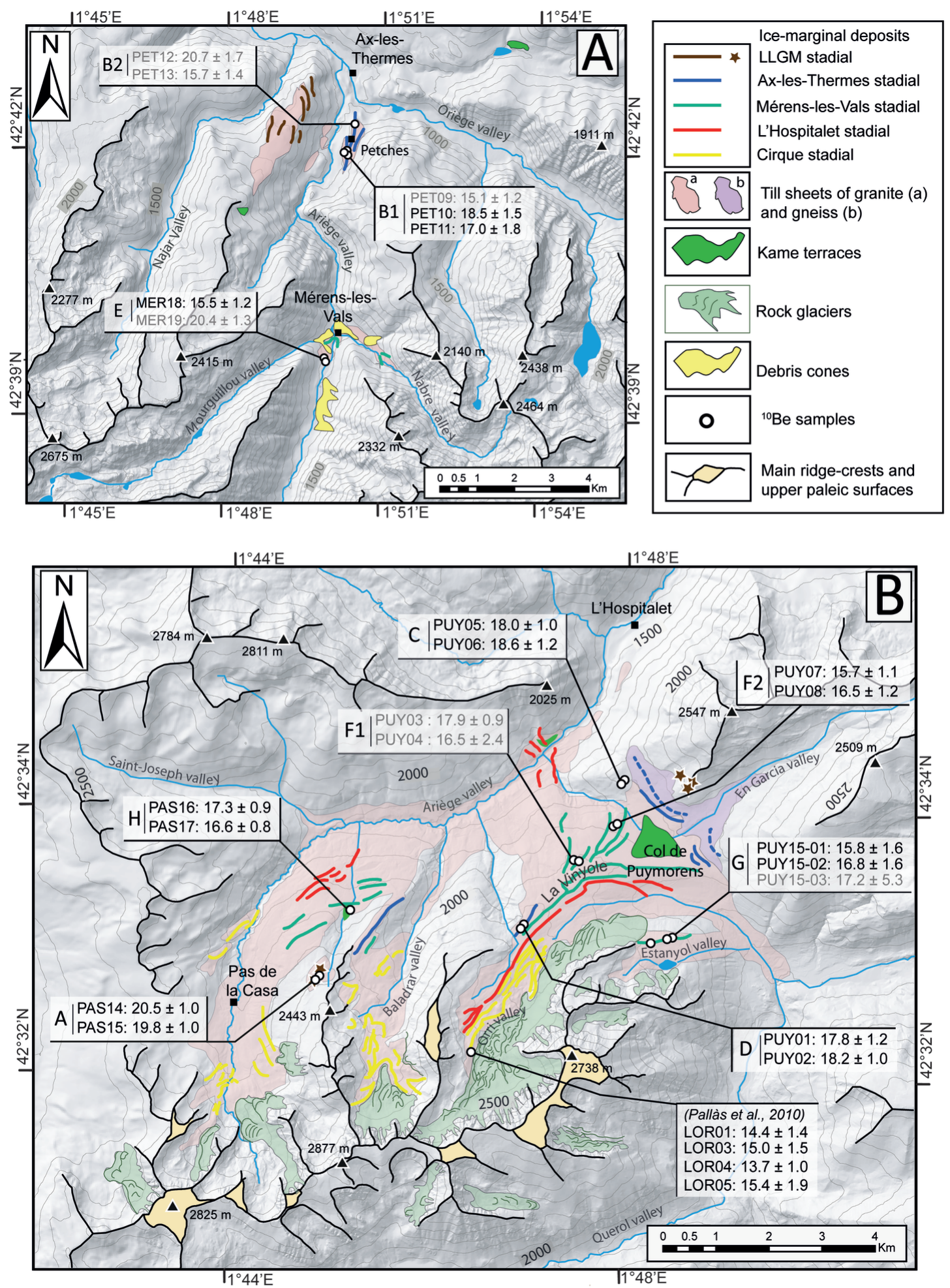
A
B
N
1°45'E
1°48'E
1°51'E
1°54'E
42°42'N
42°39'N
Ax-les-Thermes
Petches
Mérens-les-Vals
Oriège valley
Ariège valley
Najar Valley
Mourguillou valley
Nabre valley
B2 | PET12: 20.7 ± 1.7
PET13: 15.7 ± 1.4
B1 | PET09: 15.1 ± 1.2
PET10: 18.5 ± 1.5
PET11: 17.0 ± 1.8
E | MER18: 15.5 ± 1.2
MER19: 20.4 ± 1.3
1911 m
2277 m
2415 m
2140 m
2438 m
2464 m
2332 m
2675 m
1000
1500
2000
0 0.5 1 2 3 4 Km
Ice-marginal deposits
LLGM stadial
Ax-les-Thermes stadial
Mérens-les-Vals stadial
L'Hospitalet stadial
Cirque stadial
a
b
Till sheets of granite (a) and gneiss (b)
Kame terraces
Rock glaciers
Debris cones
10Be samples
Main ridge-crests and upper paleic surfaces
1°44'E
1°48'E
42°34'N
42°32'N
L'Hospitalet
C | PUY05: 18.0 ± 1.0
PUY06: 18.6 ± 1.2
F1 | PUY03 : 17.9 ± 0.9
PUY04 : 16.5 ± 2.4
F2 | PUY07: 15.7 ± 1.1
PUY08: 16.5 ± 1.2
H | PAS16: 17.3 ± 0.9
PAS17: 16.6 ± 0.8
G | PUY15-01: 15.8 ± 1.6
PUY15-02: 16.8 ± 1.6
PUY15-03: 17.2 ± 5.3
A | PAS14: 20.5 ± 1.0
PAS15: 19.8 ± 1.0
D | PUY01: 17.8 ± 1.2
PUY02: 18.2 ± 1.0
(Pallàs et al., 2010)
LOR01: 14.4 ± 1.4
LOR03: 15.0 ± 1.5
LOR04: 13.7 ± 1.0
LOR05: 15.4 ± 1.9
2784 m
2811 m
2025 m
2547 m
2509 m
2443 m
2738 m
2877 m
2825 m
Saint-Joseph valley
Ariège valley
En Garcia valley
La Vinyole
Col de Puymorens
Pas de la Casa
Baladrar valley
Estanyol valley
Querol valley
2000
2500

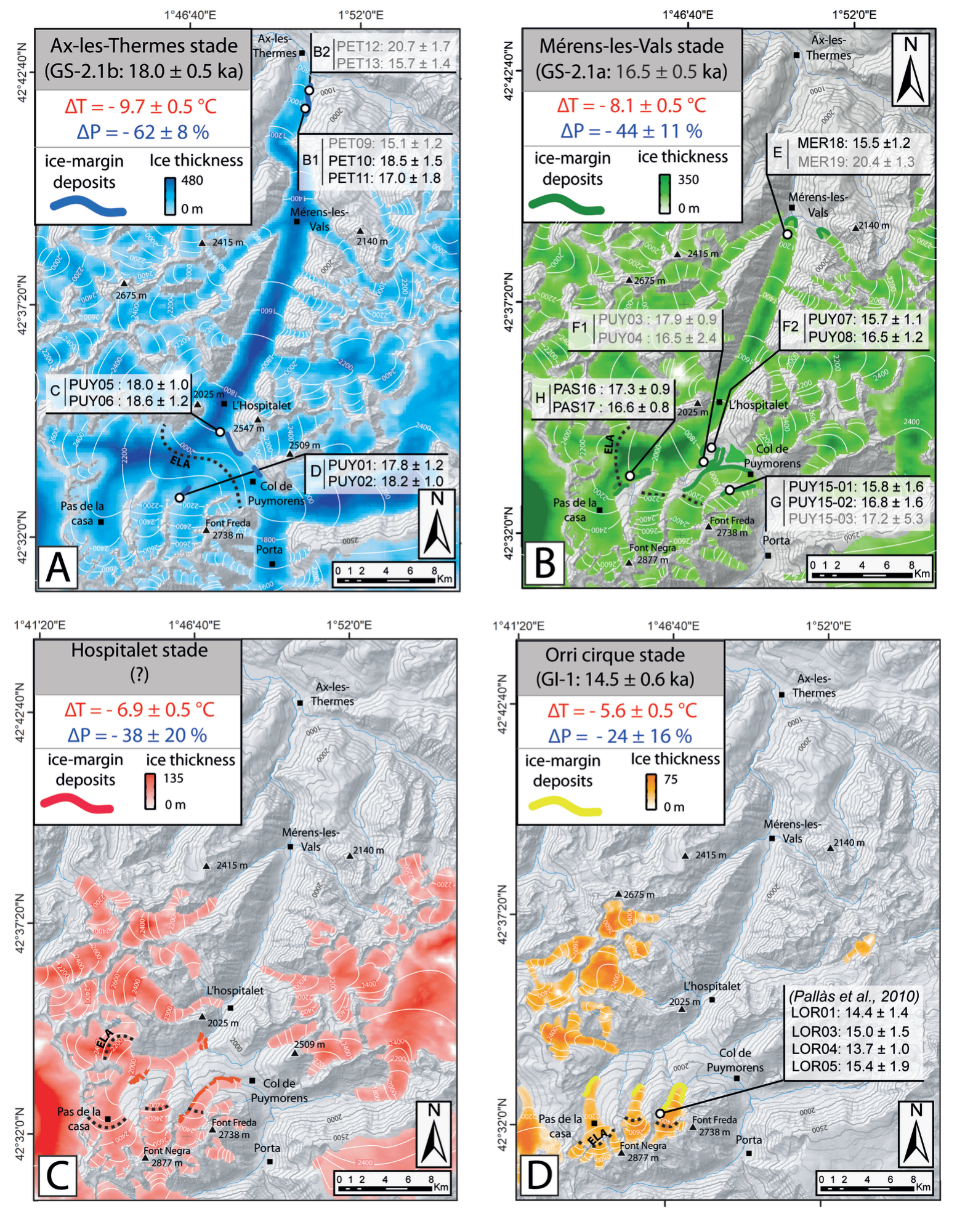
Ax-les-Thermes stade
(GS-2.1b: 18.0 ± 0.5 ka)
ΔT = - 9.7 ± 0.5 °C
ΔP = - 62 ± 8 %
ice-margin deposits
Ice thickness
480
0 m
B2 PET12: 20.7 ± 1.7
PET13: 15.7 ± 1.4
B1 PET09: 15.1 ± 1.2
PET10: 18.5 ± 1.5
PET11: 17.0 ± 1.8
C PUY05 : 18.0 ± 1.0
PUY06 : 18.6 ± 1.2
D PUY01: 17.8 ± 1.2
PUY02: 18.2 ± 1.0
ELA
A
Mérens-les-Vals stade
(GS-2.1a: 16.5 ± 0.5 ka)
ΔT = - 8.1 ± 0.5 °C
ΔP = - 44 ± 11 %
ice-margin deposits
ice thickness
350
0 m
E MER18: 15.5 ±1.2
MER19: 20.4 ± 1.3
F1 PUY03 : 17.9 ± 0.9
PUY04 : 16.5 ± 2.4
F2 PUY07: 15.7 ± 1.1
PUY08: 16.5 ± 1.2
H PAS16 : 17.3 ± 0.9
PAS17 : 16.6 ± 0.8
G PUY15-01: 15.8 ± 1.6
PUY15-02: 16.8 ± 1.6
PUY15-03: 17.2 ± 5.3
B
Hospitalet stade
(?)
ΔT = - 6.9 ± 0.5 °C
ΔP = - 38 ± 20 %
ice-margin deposits
ice thickness
135
0 m
C
Orri cirque stade
(GI-1: 14.5 ± 0.6 ka)
ΔT = - 5.6 ± 0.5 °C
ΔP = - 24 ± 16 %
ice-margin deposits
Ice thickness
75
0 m
(Pallàs et al., 2010)
LOR01: 14.4 ± 1.4
LOR03: 15.0 ± 1.5
LOR04: 13.7 ± 1.0
LOR05: 15.4 ± 1.9
D
Ax-les-Thermes
Mérens-les-Vals
L'Hospitalet
Col de Puymorens
Pas de la casa
Font Freda 2738 m
Font Negra 2877 m
Porta
2140 m
2415 m
2675 m
2025 m
2547 m
2509 m
1°41'20"E
1°46'40"E
1°52'0"E
42°42'40"N
42°37'20"N
42°32'0"N
N
0 1 2 4 6 8 Km

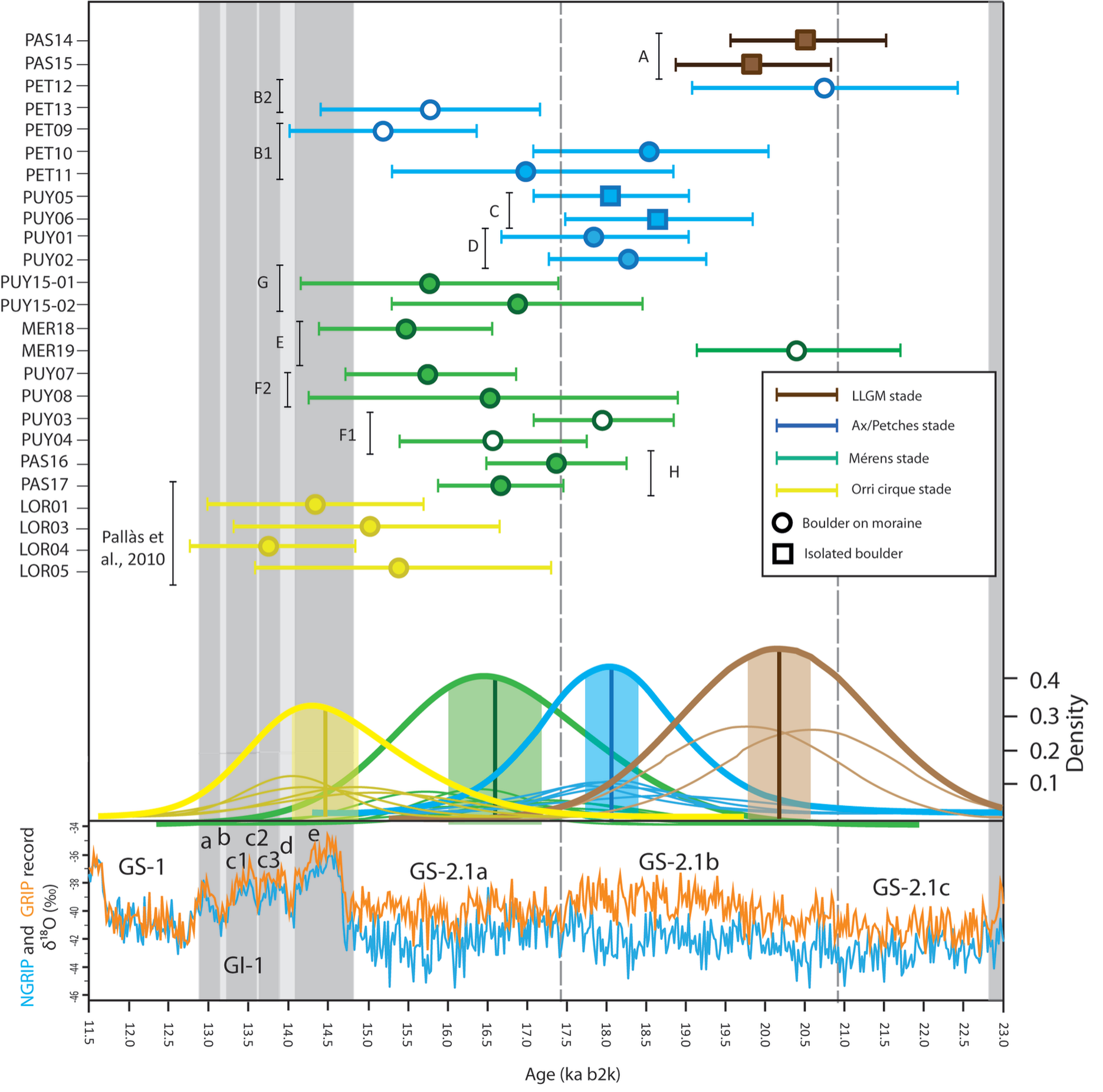
PAS14
PAS15
PET12
PET13
PET09
PET10
PET11
PUY05
PUY06
PUY01
PUY02
PUY15-01
PUY15-02
MER18
MER19
PUY07
PUY08
PUY03
PUY04
PAS16
PAS17
LOR01
LOR03
LOR04
LOR05
Pallàs et al., 2010
A
B2
B1
C
D
G
E
F2
F1
H
LLGM stade
Ax/Petches stade
Mérens stade
Orri cirque stade
Boulder on moraine
Isolated boulder
Density
0.4
0.3
0.2
0.1
NGRIP and GRIP record
δ18O (‰)
-34
-36
-38
-40
-42
-44
-46
GS-1
a b c2 c1 c3 d e
GS-2.1a
GS-2.1b
GS-2.1c
GI-1
11.5
12.0
12.5
13.0
13.5
14.0
14.5
15.0
15.5
16.0
16.5
17.0
17.5
18.0
18.5
19.0
19.5
20.0
20.5
21.0
21.5
22.0
22.5
23.0
Age (ka b2k)

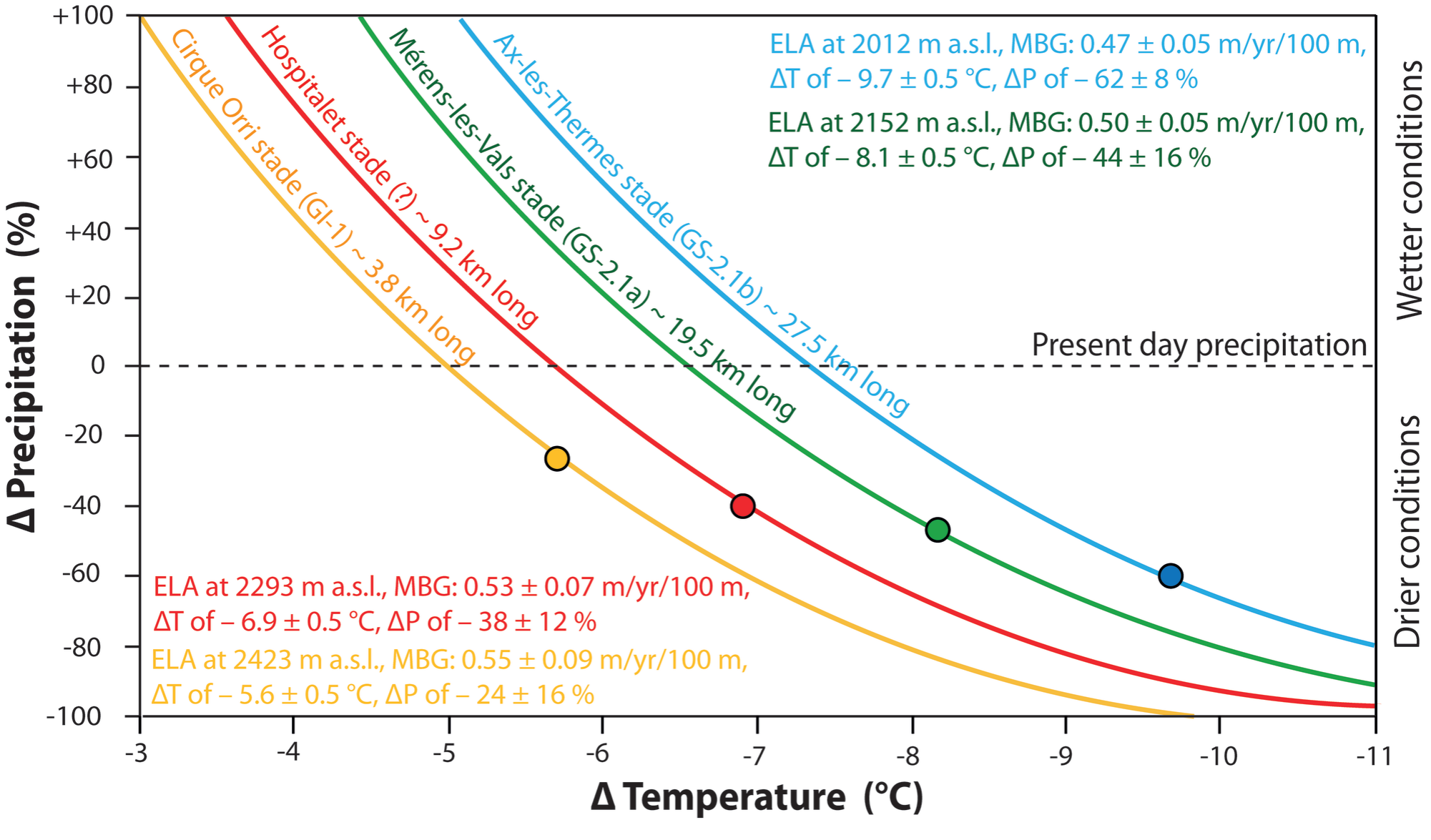
ELA at 2012 m a.s.l., MBG: 0.47 ± 0.05 m/yr/100 m,
ΔT of – 9.7 ± 0.5 °C, ΔP of – 62 ± 8 %
ELA at 2152 m a.s.l., MBG: 0.50 ± 0.05 m/yr/100 m,
ΔT of – 8.1 ± 0.5 °C, ΔP of – 44 ± 16 %
Ax-les-Thermes stade (GS-2.1b) ~ 27.5 km long
Mérens-les-Vals stade (GS-2.1a) ~ 19.5 km long
Hospitalet stade (?) ~ 9.2 km long
Cirque Orri stade (GI-1) ~ 3.8 km long
Present day precipitation
ELA at 2293 m a.s.l., MBG: 0.53 ± 0.07 m/yr/100 m,
ΔT of – 6.9 ± 0.5 °C, ΔP of – 38 ± 12 %
ELA at 2423 m a.s.l., MBG: 0.55 ± 0.09 m/yr/100 m,
ΔT of – 5.6 ± 0.5 °C, ΔP of – 24 ± 16 %
Wetter conditions
Drier conditions
Δ Precipitation (%)
+100
+80
+60
+40
+20
0
-20
-40
-60
-80
-100
-3
-4
-5
-6
-7
-8
-9
-10
-11
Δ Temperature (°C)

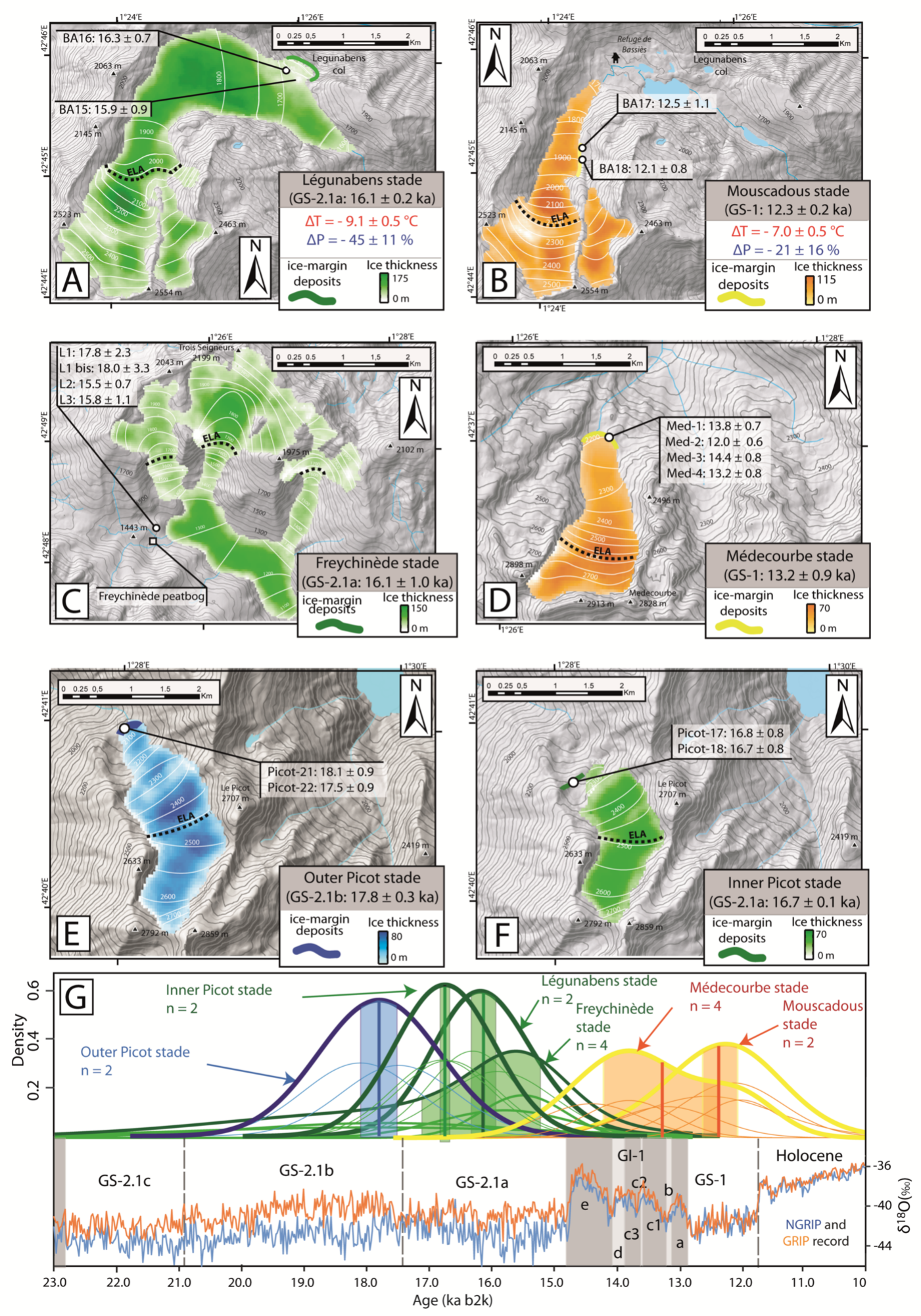
A
BA16: 16.3 ± 0.7
BA15: 15.9 ± 0.9
Légunabens stade
(GS-2.1a: 16.1 ± 0.2 ka)
ΔT = - 9.1 ± 0.5 °C
ΔP = - 45 ± 11 %
ice-margin deposits
Ice thickness
175
0 m
B
BA17: 12.5 ± 1.1
BA18: 12.1 ± 0.8
Mouscadous stade
(GS-1: 12.3 ± 0.2 ka)
ΔT = - 7.0 ± 0.5 °C
ΔP = - 21 ± 16 %
115
C
L1: 17.8 ± 2.3
L1 bis: 18.0 ± 3.3
L2: 15.5 ± 0.7
L3: 15.8 ± 1.1
Freychinède peatbog
Freychinède stade
(GS-2.1a: 16.1 ± 1.0 ka)
150
D
Med-1: 13.8 ± 0.7
Med-2: 12.0 ± 0.6
Med-3: 14.4 ± 0.8
Med-4: 13.2 ± 0.8
Médecourbe stade
(GS-1: 13.2 ± 0.9 ka)
70
E
Picot-21: 18.1 ± 0.9
Picot-22: 17.5 ± 0.9
Outer Picot stade
(GS-2.1b: 17.8 ± 0.3 ka)
80
F
Picot-17: 16.8 ± 0.8
Picot-18: 16.7 ± 0.8
Inner Picot stade
(GS-2.1a: 16.7 ± 0.1 ka)
ELA
Le Picot
Médecourbe
Refuge de Bassiès
Trois Seigneurs
Legunabens col
G
Density
Inner Picot stade
n = 2
Outer Picot stade
n = 2
Légunabens stade
n = 2
Freychinède
stade
n = 4
Médecourbe stade
n = 4
Mouscadous
stade
n = 2
GS-2.1c
GS-2.1b
GS-2.1a
GI-1
GS-1
Holocene
NGRIP and
GRIP record
δ18O(‰)
Age (ka b2k)

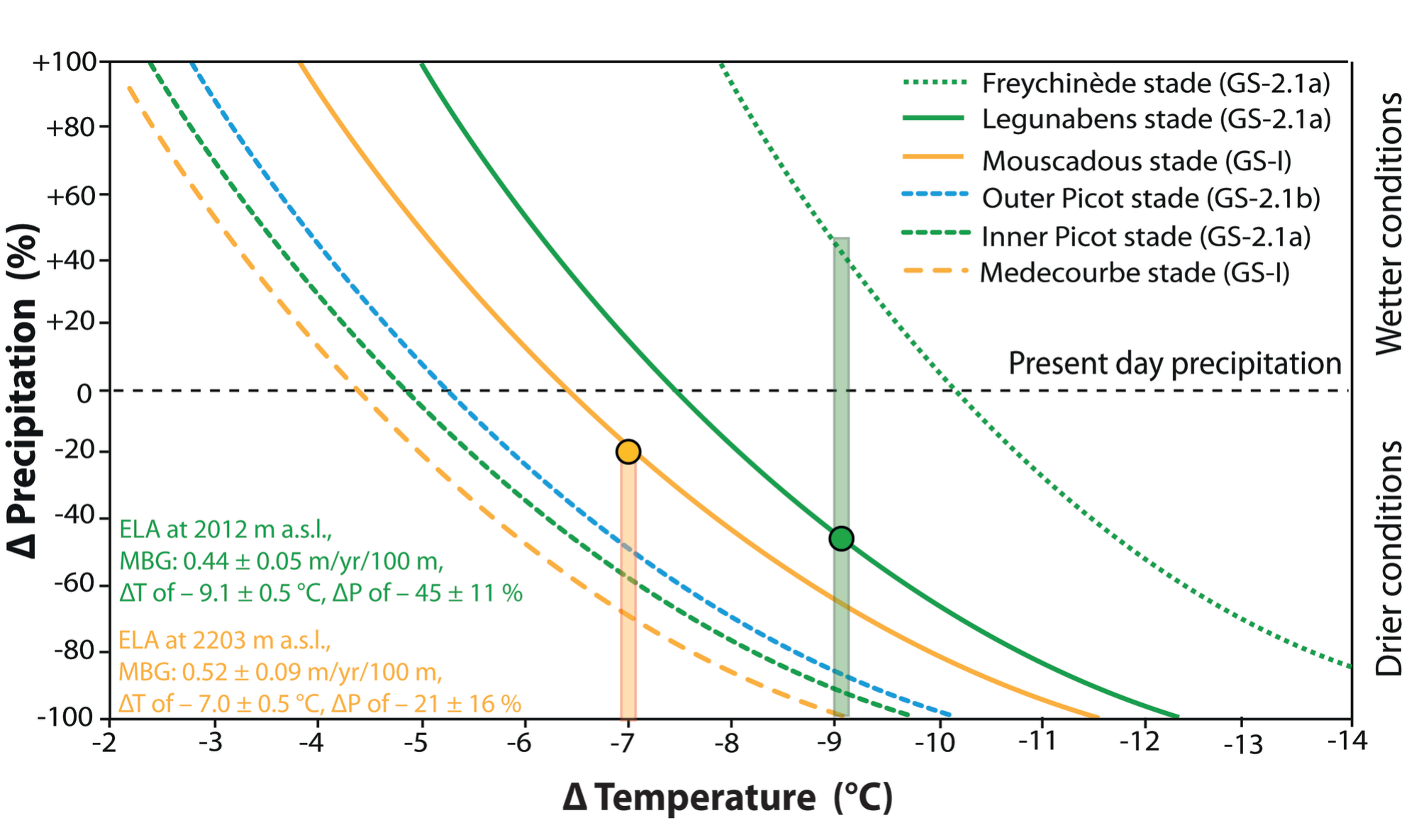
Freychinède stade (GS-2.1a)
Legunabens stade (GS-2.1a)
Mouscadous stade (GS-I)
Outer Picot stade (GS-2.1b)
Inner Picot stade (GS-2.1a)
Medecourbe stade (GS-I)
Present day precipitation
Wetter conditions
Drier conditions
ELA at 2012 m a.s.l.,
MBG: 0.44 ± 0.05 m/yr/100 m,
ΔT of – 9.1 ± 0.5 °C, ΔP of – 45 ± 11 %
ELA at 2203 m a.s.l.,
MBG: 0.52 ± 0.09 m/yr/100 m,
ΔT of – 7.0 ± 0.5 °C, ΔP of – 21 ± 16 %
Δ Precipitation (%)
+100
+80
+60
+40
+20
0
-20
-40
-60
-80
-100
-2
-3
-4
-5
-6
-7
-8
-9
-10
-11
-12
-13
-14
Δ Temperature (°C)

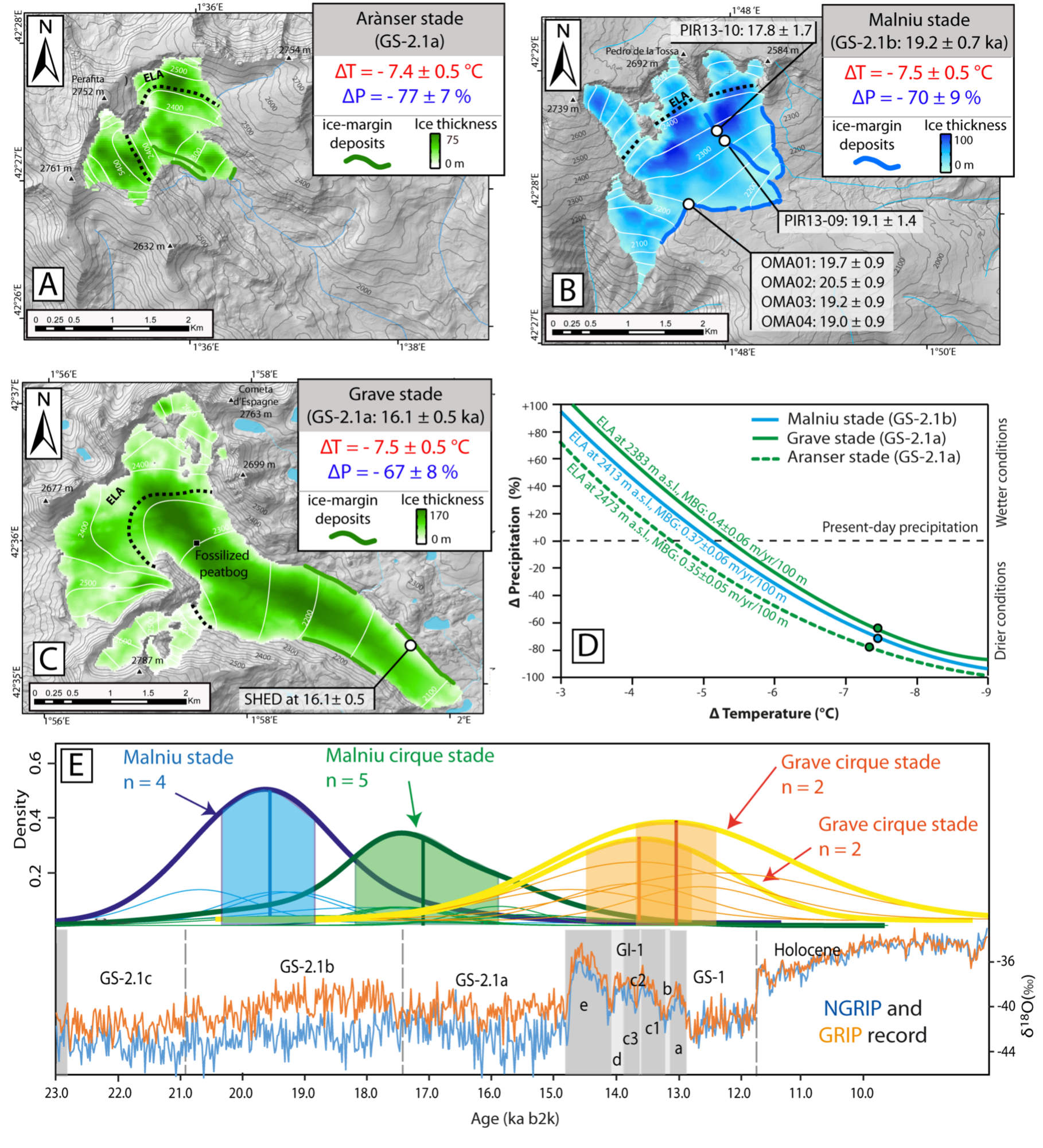
A
Aránser stade
(GS-2.1a)
ΔT = - 7.4 ± 0.5 °C
ΔP = - 77 ± 7 %
ice-margin deposits
Ice thickness
75
0 m
ELA
Perafita
2752 m
2754 m
2761 m
2632 m
B
Malniu stade
(GS-2.1b: 19.2 ± 0.7 ka)
ΔT = - 7.5 ± 0.5 °C
ΔP = - 70 ± 9 %
ice-margin deposits
Ice thickness
100
0 m
PIR13-10: 17.8 ± 1.7
PIR13-09: 19.1 ± 1.4
OMA01: 19.7 ± 0.9
OMA02: 20.5 ± 0.9
OMA03: 19.2 ± 0.9
OMA04: 19.0 ± 0.9
Pedro de la Tossa
2692 m
2584 m
2739 m
C
Grave stade
(GS-2.1a: 16.1 ± 0.5 ka)
ΔT = - 7.5 ± 0.5 °C
ΔP = - 67 ± 8 %
ice-margin deposits
Ice thickness
170
0 m
Cometa d'Espagne
2763 m
2699 m
2677 m
2787 m
Fossilized peatbog
SHED at 16.1± 0.5
D
Malniu stade (GS-2.1b)
Grave stade (GS-2.1a)
Aranser stade (GS-2.1a)
ELA at 2383 m a.s.l., MBG: 0.4±0.06 m/yr/100 m
ELA at 2413 m a.s.l., MBG: 0.37±0.06 m/yr/100 m
ELA at 2473 m a.s.l., MBG: 0.35±0.05 m/yr/100 m
Present-day precipitation
Δ Precipitation (%)
Δ Temperature (°C)
Wetter conditions
Drier conditions
E
Malniu stade
n = 4
Malniu cirque stade
n = 5
Grave cirque stade
n = 2
Grave cirque stade
n = 2
Density
GS-2.1c
GS-2.1b
GS-2.1a
GI-1
GS-1
Holocene
NGRIP and
GRIP record
Age (ka b2k)
δ18O(‰)

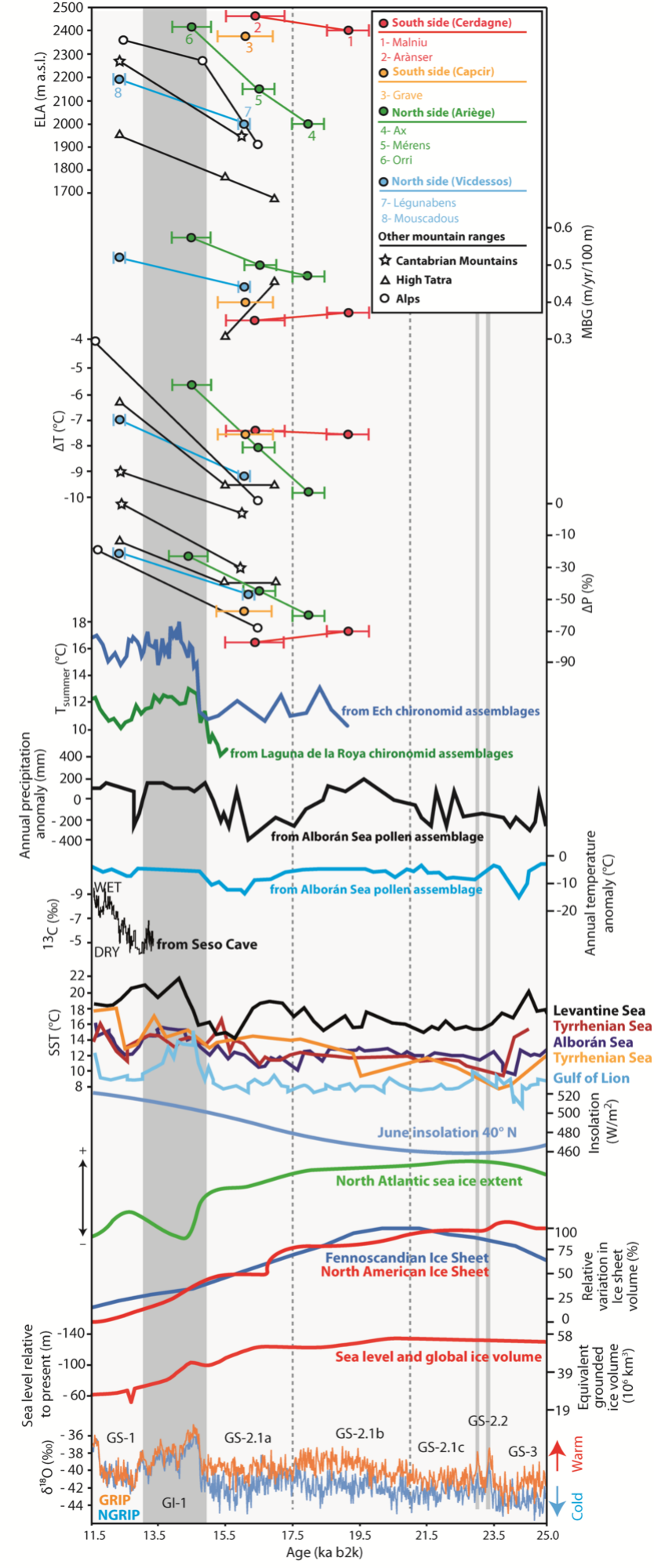
South side (Cerdagne)
1- Malniu
2- Aránser
South side (Capcir)
3- Grave
North side (Ariège)
4- Ax
5- Mérens
6- Orri
North side (Vicdessos)
7- Léguanabens
8- Mouscadous
Other mountain ranges
Cantabrian Mountains
High Tatra
Alps
ELA (m a.s.l.)
MBG (m/yr/100 m)
ΔT (°C)
ΔP (%)
T summer (°C)
from Ech chironomid assemblages
from Laguna de la Roya chironomid assemblages
Annual precipitation anomaly (mm)
from Alborán Sea pollen assemblage
Annual temperature anomaly (°C)
from Alborán Sea pollen assemblage
WET
DRY
13C (‰)
from Seso Cave
SST (°C)
Levantine Sea
Tyrrhenian Sea
Alborán Sea
Tyrrhenian Sea
Gulf of Lion
June insolation 40° N
Insolation (W/m2)
North Atlantic sea ice extent
Fennoscandian Ice Sheet
North American Ice Sheet
Relative variation in Ice sheet volume (%)
Sea level and global ice volume
Sea level relative to present (m)
Equivalent grounded ice volume (10⁶ km³)
GS-1
GS-2.1a
GS-2.1b
GS-2.1c
GS-2.2
GS-3
GI-1
δ18O (‰)
GRIP
NGRIP
Warm
Cold
Age (ka b2k)

Table 1. Location of cosmogenic ^{10}Be samples (Ariège valley)

Glacial stade	Sample site (see Fig. 4)	Sample code	Lithology	Latitude [1] (dec. deg.)	Longitude [1] (dec. deg.)	Altitude (m a.s.l.)
Close to LLGM	A	PAS14	Granite	42.5452	1.7477	2280
		PAS15	Granite	42.5455	1.7480	2280
Ax-les-Thermes	B1	PET09	Gneiss	42.7002	1.8386	930
		PET10	Gneiss	42.6994	1.8388	930
		PET11	Gneiss	42.7000	1.8380	917
	B2	PET12	Gneiss	42.7069	1.8405	928
		PET13	Gneiss	42.7069	1.8405	918
	C	PUY05	Granite	42.5708	1.7994	1922
		PUY06	Granite	42.5702	1.7988	1917
	D	PUY01	Granite	42.5519	1.7822	2144
		PUY02	Granite	42.5525	1.7827	2131
Mérens-les-Vals	E	MER18	Gneiss	42.6511	1.8325	1116
		MER19	Gneiss	42.6513	1.8322	1114
	F1	PUY03	Granite	42.5608	1.7911	2001
		PUY04	Granite	42.5605	1.7919	2000
	F2	PUY07	Granite	42.5650	1.7977	1894
		PUY08	Granite	42.5652	1.7983	1888
	G	PUY15-01	Granite	42.5511	1.8077	2054
		PUY15-02	Granite	42.5508	1.8071	2072
		PUY15-03	Granite	42.5503	1.8041	2092
	H	PAS16	Granite	42.5544	1.7530	2040
		PAS17	Granite	42.5541	1.7533	2040

Note. [1] Ellipsoid of reference: WGS84

Table 2. Cosmogenic ^{10}Be surface data from the upper Ariège catchment

Sampling site (see Fig. 4)	Sample code	Scaling factor	Topographic shielding factor	Snow (cm/yr)	Snow shielding	[^{10}Be] (10^5 at/g)	Exposure age [1] ($*10^3$ yr ± 1 sigma)	Exposure age [2] ($*10^3$ yr ± 1 sigma)
A	PAS14	5.69	0.99	55	0.91	4.37 ± 0.15	18.8 ± 0.9	20.5 ± 1.0
	PAS15	5.68	0.99	55	0.91	4.22 ± 0.13	18.2 ± 0.9	19.8 ± 0.9
B1	PET09	2.06	0.99	0	1	1.28 ± 0.09	15.12 ± 1.2	15.1 ± 1.2
	PET10	2.09	0.99	0	1	1.58 ± 0.12	18.48 ± 1.5	18.4 ± 1.5
	PET11	2.05	0.99	0	1	1.43 ± 0.15	16.97 ± 1 .7	16.9 ± 1 .7
B2	PET12	2.10	0.98	0	1	1.77 ± 0.13	20.77 ± 1.7	20.7 ± 1.7
	PET13	2.05	0.98	0	1	1.31 ± 0.11	15.75 ± 1.3	15.7 ± 1.3
C	PUY05	4.40	0.99	30	0.95	3.10 ± 0.13	17.2 ± 1.0	18.0 ± 1.0
	PUY06	4.39	0.99	30	0.95	3.19 ± 0.16	17.7 ± 1.1	18.5 ± 1.1
D	PUY01	5.13	0.99	45	0.93	3.5 ± 0.20	16.6 ± 1.1	17.8 ± 1.1
	PUY02	5.09	0.99	45	0.93	3.5 ± 0.16	17.0 ± 1.0	18.1 ± 1.0
E	MER18	2.39	0.97	0	1	1.49 ± 0.10	15.51 ± 1.1	15.5 ± 1.1
	MER19	2.43	0.97	0	1	2.0 ± 0.11	20.44 ± 1.3	20.4 ± 1.3
F1	PUY03	4.65	0.99	35	0.94	3.2 ± 0.12	16.9 ± 0.9	17.8 ± 0.9
	PUY04	4.62	0.99	35	0.94	2.9 ± 0.44	15.6 ± 2.3	16.5 ± 2.3
F2	PUY07	4.40	0.99	30	0.96	2.65 ± 0.15	15.2 ± 1.0	15.7 ± 1.0
	PUY08	4.27	0.99	30	0.96	2.79 ± 0.18	15.9 ± 1.2	16.5 ± 1.2
G	PUY15-01	4.84	0.99	40	0.93	2.5 ± 0.30	15.0 ± 1.5	15.8 ± 1.6
	PUY15-02	4.80	0.99	40	0.93	3.6 ± 0.30	15.6 ± 1.5	16.8 ± 1.6
	PUY15-03	4.94	0.99	40	0.93	3.2 ± 1.08	16.1 ± 5.0	17.7 ± 5.5
H	PAS16	4.75	0.99	38	0.95	3.10 ± 0.10	15.9 ± 0.8	16.6 ± 0.8
	PAS17	4.76	0.99	38	0.95	3.22 ± 0.13	16.5 ± 0.9	17.3 ± 0.9

Notes: [1] without snow shielding; [2] with snow shielding. Outliers highlighted in gray.

Table 3. Synthesis of glaciologic and climatic reconstructions of east-Pyrenean LGIT glacial stades

Location	**Chronological data**			**Glaciological reconstructions**				**Climatic reconstructions**	
Relative position within mountain range	INTIMATE stratigraphy	Local glacial stade	Age (ka ± 1 sigma)	Glacier length (km)	Area above ELA (km^2)	ELA (m a.s.l.)	Mass-balance gradient ($m.yr^{-1}.100\ m^{-1}$)	ΔT (°C)	ΔP (%)
North	GS-2.1b	Ax-les-Thermes	18.0 ± 0.5	27.5	90.7	2012	0.47 ± 0.05	–9.7 ± 0.5	–62 ± 8
North		Outer Picot	17.8 ± 0.3	2.6	No data	2425[1]	No data	No data	No data
South		Malniu	19.2 ± 0.7	3.1	2.1	2413	0.37 ± 0.06	–7.5 ± 0.5	–70 ± 9
North	GS-2.1a	Mérens-les-Vals	16.5 ± 0.5	19.5	25.3	2152	0.50 ± 0.05	–8.1 ± 0.5	–44 ± 11
North		Freychinède	16.7 ± 1.0	4.9	3.6	1700[1]	0.65 ± 0.09	–9.1 ± 0.5 [2]	+45 ± 25 [4]
North		Légunabens	16.1 ± 0.2	6.6	4.4	2012	0.44 ± 0.05	–9.1 ± 0.5	–45 ± 11
North		Inner Picot	16.7 ± 0.1	1.9	0.4	2449[1]	0.23 ± 0.04	–9.1 ± 0.5 [2]	–80 ± 5 [4]
South		Aránser	Indirectly dated	2.4	0.5	2473	0.35 ± 0.05	–7.4 ± 0.5	–77 ± 7
South		Grave	16.1 ± 0.5	6.5	3.8	2383	0.40 ± 0.06	–7.5 ± 0.5	–67 ± 8
North	No data	Hospitalet	No data	9.2	16	2293	0.53 ± 0.07	–6.9 ± 0.5	–38 ± 12
North	GI-1	Cirque Orri	14.5 ± 0.6	3.8	2.8	2423	0.55 ± 0.09	–5.6 ± 0.5	–24 ± 16
North	GS-1	Mouscadous	12.3 ± 0.2	3.4	2.1	2203	0.52 ± 0.09	– 7.0 ± 0.5	–21 ± 16
North		Médecourbe	13.2 ± 0.9	1.6	0.4	2525[1]	0.41 ± 0.03	– 7.0 ± 0.5[3]	–60 ± 7[4]

Notes. [1] ELA calculated using the AABR method (Balance ratio of 1.59; Rea, 2009). [2] ΔT value obtained for Légunabens glacial stade. [3] ΔT value obtained for Medecourbe glacial stade. [4] ΔP value modeled on the basis of a ΔT value obtained from an adjacent catchment during the same glacial stade.